A compliant and low-expansion 2-phase micro-architectured material, with potential application to solid-state Li-ion batteries

Ying Zhao[a,b], Vikram S. Deshpande[b], Norman A. Fleck[b,*]

[a]*Department of Aerospace Engineering and Applied Mechanics, Tongji University, Shanghai 200092, China*
[b]*Department of Engineering, University of Cambridge, Trumpington Street, CB2 1PZ Cambridge, UK*

Abstract

A two-phase 2D lattice material is identified that possesses both a high macroscopic compliance and a low macroscopic coefficient of thermal expansion. The macroscopic effective properties of the lattice are analysed and the features that give high macroscopic compliance and low macroscopic actuation strain are identified. A detailed case study is presented to explore the potential of the lattice for use as a composite cathode in a solid-state Li-ion battery, taking into account the swelling of the active cathode material upon lithiation. A design map is developed to reveal the competition between battery capacity and degradation due to fracture of the composite cathode. The intent is to identify promising battery topologies and compositions by overcoming the usual problems associated with cathode swell during charge and discharge.

Keywords: Lithium-ion battery, multi-phase lattice material, Composite electrode, Lattice material, All-solid-state battery

1. Introduction

There has been significant recent interest in the development of lattice materials that possess high macroscopic stiffness and low thermal expansion coefficient for structural applications at high temperatures (such as hypersonics). Such lattices comprise 2 distinct phases in addition to porosity, and each phase has dissimilar elastic moduli and thermal expansion coefficients. In contrast, less attention has been paid to the invention of two phase lattices of

*Corresponding author
Email addresses: 19531@tongji.edu.cn (Ying Zhao), vsd20@cam.ac.uk (Vikram S. Deshpande), naf1@cam.ac.uk (Norman A. Fleck)

high macroscopic compliance and low macroscopic thermal expansion; we shall show that the problem of electrode swell in solid-state batteries demands the invention of composites that can accommodate large swelling/contraction of the active material upon charge and discharge, along with a high macroscopic compliance in order to minimise swelling-induced self-stress in the battery.

The lattice topology proposed by Steeves et al. (2007, 2009) achieves tunable thermal macroscopic expansion, but has a high macroscopic stiffness. In contrast, Lakes' lattices (Lakes, 1996, 2007) have tunable thermal expansions and can exhibit high compliance. However, these structures require unsymmetric beams to be constructed in an alternating manner, making the lattices difficult to manufacture. Sigmund and Torquato (1996, 1997) have used topology optimization to identify topologies of high macroscopic compliance and low thermal expansion coefficient. Again, these structures comprise irregular patterns and, in common with Lakes' lattices, are a challenge to manufacture.

1.1. Motivation of study: application of 2-phase lattice to solid-state Li-ion battery

Lattice materials of high compliance and low thermal expansion show promise as the composite cathode of a solid-state Li-ion battery. The composite cathode comprises a solid ceramic electrolyte to allow for the transport of Li ions and a ceramic electrode material (the active material) that swells significantly upon lithiation. Swelling due to the absorption of Li ions is analogous to thermal expansion. Currently, one limit to the energy storage capacity of Li-ion batteries is the fracture of electrodes by stresses induced by non-uniform lithiation during charge/discharge. Thus, there is a need to invent topologies that can accommodate the large swell of the active electrode material without generation of large self-stresses. The aim of the present study is to report on the effective macroscopic properties of a candidate compliant and swell-resistant topology and to scope-out its potential for use as a cathode in a Li-ion battery. The geometry of interest is sketched in Fig. 1.

The conceptual design in the present paper is that of a compliant battery element and not a structural battery element. The aim is to design a micro-architectured electrode with two advantageous features: (i) it undergoes small macroscopic straining upon lithiation/delithiation of the strut elements, and (ii) is has a low passive stiffness, such that it generates low levels of residual stress when the macroscopic straining is constrained by neighbouring elements. In

contrast, a lattice of low macroscopic actuation strain, but stiff in the passive state, will generate much larger levels of residual stress when it undergoes a small macroscopic actuation stain and is restrained against such expansion by neighbouring elements. Stiff lattices of low macroscopic actuation strain have been invented (see for example Steeves et al. (2007)) and have the potential for use in a structural battery element, but the present concept has the advantage of ensuring that the stress levels generated by lithiation/delithiation are low regardless of the level of external constraint.

Electrode elements have also been developed that are based on a monolithic lattice, such as a hexagonal lattice of silicon, see for example the analysis by Bhandakkar and Johnson (2012). This geometry is simpler to manufacture than the two-phase lattice contemplated in the present study, but it suffers from the disadvantage that the macroscopic strain equals the local swelling strain due to lithiation/delithiation. All monolithic lattices, such as the fully triangulated lattice and the Kagome lattice share this drawback. When the macroscopic strain is constrained by neighbouring elements, residual stresses are induced and the level of stress is dictated by the passive stiffness of the lattice in relation to that of neighbouring elements. The hexagonal lattice is more compliant than that of the fully triangulated and Kagome lattices, and so the level of induced residual stress is less. Additional stress relieving mechanisms can come into play such as elastic or elastic-plastic buckling of the lattices when the induced (compressive) residual stress is of sufficient magnitude. This scenario has been analysed by Bhandakkar and Johnson (2012), for example.

In broad terms, the two-phase lattice of the present study has two major merits: it generates a low value of macroscopic actuation strain, and it has a low passive stiffness, thereby inducing a low level of residual stress when constrained by neighbouring elements.

A typical solid-state battery consists of a lithium metal anode, a solid-state electrolyte which acts as a separator (to allow Li ions to migrate but to insulate against electron flow), and a composite cathode (Janek and Zeier, 2016). Typical composite cathodes comprise active particles ($61\,\%$ wt), solid electrolyte ($36\,\%$ wt) and an electron-conducting powder ($3\,\%$ wt) (Kato et al., 2016). Such solid-state batteries are fire-proof, and are stable against both mechanical and thermal loadings (Famprikis et al., 2019).

A number of candidate electrolytes are under development: *oxides* such as lithium lan-

thanum titanate (LLTO) and lithium lanthanum zirconium oxide (LLZO), *phosphates* such as lithium aluminum titanium phosphate (LATP), and *sulfide-based* electrolytes such as $\beta - \mathrm{Li_3PS_4}$ and lithium phosphorus sulfide chloride ($\mathrm{Li_6PS_5Cl}$). These ceramic electrolytes exhibit a higher conductivity to Li ions than polymer electrolytes; however, they also possess a much higher elastic modulus and a lower fracture toughness, as shown in Table 1. Consequently, ceramic electrolytes and ceramic composite cathodes may crack due to cathode swell upon lithiation.

Ceramic cathodes made from lithium nickel cobalt aluminium oxide (NCA) or lithium nickel manganese cobalt oxide (NMC) possess a specific energy density as high as $200\,\mathrm{mA\,h\,g^{-1}}$ but undergo a fractional volume change on the order of $5\,\%$ upon lithiation (Koerver et al., 2018). Other cathode material candidates also swell significantly upon lithiation (Fig. 2). Moreover, most cathode materials possess a high value of Young's modulus and a low value of fracture toughness, as summarized in Table 2. The problem of stress generation by strain mismatch between electrolyte and cathode can be alleviated by designing the topology of the composite cathode such that it has a high macroscopic compliance and a low macroscopic expansion strain upon lithiation.

Table 1: Mechanical properties and lithium ion conductivity of solid electrolytes. (Refs: (a) Wolfenstine et al. (2018); (b) Fergus (2010); (c) Wolfenstine et al. (2013); (d) Aono et al. (1989); (e) Deng et al. (2016); (f) Bachman et al. (2016); (g) McGrogan et al. (2017); (h) Liu et al. (2013).)

Solid Eletrolyte	Young's modulus $[\mathrm{GPa}]$	Fracture toughness $[\mathrm{MPa\,m^{1/2}}]$	Ion conductivity $[\mathrm{S\,cm^{-1}}]$
Perovskite LLTO	200 (a)	1 (a)	1×10^{-4} (b)
Garnet LLZO	150 (c)	1 (c)	4×10^{-4} (b)
NaSICON LATP	115 (a)	1 (a)	1×10^{-3} (d)
Argyrodite $\mathrm{Li_6PS_5Cl}$	20 (e)		7×10^{-3} (f)
$\beta - \mathrm{Li_3PS_4}$	20 (g)	0.23 (g)	$> 1 \times 10^{-4}$ (g,h)

1.2. Scope of Study

In the first section of this paper, we propose a hierarchical, 2-phase, micro-architectured porous solid that is able to accommodate high actuation strains of the active material from

Table 2: Mechanical properties, lithium diffusivity and electronic conductivity of cathode materials. (Refs: (a) Qu et al. (2012); (b) Swallow et al. (2014); (c) Xia et al. (2007); (d) Park et al. (2010); (e) Xu et al. (2017); (f) Amin and Chiang (2016); (g) Woodford et al. (2013); (h) Amanieu et al. (2014).)

Cathode	Young's modulus [GPa]	Fracture toughness [$\mathrm{MPa\,m^{1/2}}$]	Li diffusivity [$\mathrm{cm^2\,s^{-1}}$]	e^- conductivity [$\mathrm{S\,cm^{-1}}$]
$LiCoO_2$	190 (a)	0.9 (a,b)	10^{-10}–10^{-8}(c,d)	10^{-4} (d)
NMC	200 (e)	0.3 (e)	10^{-10}–$10^{-9.5}$(f)	$10^{-7} - 10^{-2}$ (f)
$LiMn_2O_4$	143 (g,h)	1 (g,h)	10^{-11}–10^{-9}(d)	10^{-6} (d)

any source (such as lithiation or thermal expansion mismatch), yet exhibits a low macroscopic expansion and a low macroscopic stiffness. The macroscopic, effective properties of the 2D lattice are determined as a function of microstructure and constituent properties by an analytical analysis of the unit cell by elementary beam theory. Periodic cell, finite element analysis (again using Euler beam theory) is used to support the development of the analytical model.

In the second part of the paper, a detailed case study for the application of this composite as a cathode is presented. The lattice is optimised for both electrical and mechanical performance in order to achieve a high energy density, high power density, low internal resistance, and minimise the risk of fracture due to cyclic charge and discharge.

The authors recognise that Euler beam theory is inaccurate for a beam of slenderness ratio below 7, approximately. On the other hand, when the storage material exists as stocky beams, it is usually much stiffer than the electrolyte which exists as slender beams. Consequently, the deformation of the slender beams dominates the overall response, and Euler beam theory suffices.

2. 2-phase microarchitecture: effective properties

Consider the 2D structure as shown in Fig. 1. The active phase A expands due to an elevation in temperature, or by the absorption of Li ions. The passive support structure (electrolyte), phase B, comprises a scaffold of squares and diamonds, each of side length l. Denote the thickness of phase A by t_A, the thickness of phase B by t_B and the inclination angle by ω, as shown in Fig. 1. The volume fractions f_A of phase A, f_B of phase B and porosity of intervening air

spaces f_{air} are given by

$$f_A = \frac{t_A}{l\cos^2\omega}, \tag{1}$$

$$f_B = \frac{2t_B}{l\cos^2\omega}, \tag{2}$$

$$f_{air} = 1 - f_A - f_B = 1 - \frac{1}{\cos^2\omega}\left(\frac{t_A}{l} + \frac{2t_B}{l}\right). \tag{3}$$

Consequently, the overall relative density of the composite lattice $\bar{\rho}$ is

$$\bar{\rho} = 1 - f_{air} = \frac{t_A + 2t_B}{l\cos^2\omega}. \tag{4}$$

The dependence of these volume fractions upon bar geometry, $\bar{t}_B = t_B/l$ and t_A/t_B, is plotted in Figs. 3(a) and 3(b) for two representative angles $\omega = 0^\circ$ and $\omega = 20^\circ$, respectively. Unit cells of four representative structures are included in the figure.

A periodic cell, finite element simulation is used to obtain some useful relations between the macroscopic elastic constants, and to obtain the macroscopic thermal expansion of the 2-phase lattice. In brief, the FEAP (Taylor, 2017) finite element package is employed, and the struts of phases A and B are taken to be sufficiently slender for Euler beam theory to suffice for the prediction of macroscopic response. (This was verified by a limited number of simulations using 2D continuum elements rather than beam elements.) Analytic solutions are derived in Appendix A for the macroscopic stiffness of the 2-phase lattice under equi-biaxial and shear loadings by treating all struts as Euler beams.

We begin by summarizing the macroscopic response of the lattice. Inspection of the composite microstructure reveals that two symmetries exist: (i) 180° rotational symmetry with respect to the central points of all squares and diamonds (denoted by red dots in Fig. A1(a) of Appendix A); and (ii) gliding reflectional symmetry along lines connecting edge middle points of squares and diamonds in the x and y directions (as denoted by red dashed lines in Fig. A1(a)). Direct inspection suggests that the structure does not possess 90° rotational symmetry. However, finite element simulations reveal that if we assume inextensional Euler beam theory, the Poisson ratio in the (x,y) co-ordinate system vanishes, $\bar{\nu}_{xy} = 0$, and the in-plane moduli in the x and y directions are equal, $\bar{E}_{xx} = \bar{E}_{yy}$. The analysis of Appendix A also reveals that the the in-plane moduli in the x and y directions are equal. Consequently, the number of independent elastic constants reduce to two: the Young's moduli $\bar{E}_{xx} = \bar{E}_{yy}$ and the shear modulus $\bar{G}_{xy}$.

Let $\bar{\epsilon}^a_{xx}$ and $\bar{\epsilon}^a_{yy}$ denote the components of macroscopic strain upon imposing an actuation strain e_a in phase A and vanishing macroscopic stress, i.e. $\bar{\sigma}_{xx} = \bar{\sigma}_{yy} = \bar{\sigma}_{xy} = 0$. Then the relation between macroscopic stress $\bar{\sigma}_{ij}$ and strain $\bar{\epsilon}_{ij}$ $(i, j = x, y)$ can be written as

$$\begin{bmatrix} \bar{\sigma}_{xx} \\ \bar{\sigma}_{yy} \\ \bar{\sigma}_{xy} \end{bmatrix} = \begin{bmatrix} \bar{E}_{xx} & 0 & 0 \\ 0 & \bar{E}_{xx} & 0 \\ 0 & 0 & \bar{G}_{xy} \end{bmatrix} \begin{bmatrix} \bar{\epsilon}_{xx} - \bar{\epsilon}^a_{xx} \\ \bar{\epsilon}_{yy} - \bar{\epsilon}^a_{yy} \\ 2\bar{\epsilon}_{xy} \end{bmatrix}. \tag{5}$$

Analytical expressions for the macroscopic bulk modulus $\bar{K} = \bar{E}_{xx}/2$ and the shear modulus $\bar{G}_{xy}$ are obtained by considering two loading cases in turn: equi-biaxial loading ($\bar{\sigma}_{xx} = \bar{\sigma}_{yy} = \bar{\sigma}$, $\bar{\sigma}_{xy} = 0$), and shear loading ($\bar{\sigma}_{xx} = \bar{\sigma}_{yy} = 0$, $\bar{\sigma}_{xy} = \bar{\tau}$). The dependence of ($\bar{\epsilon}^a_{xx}$, $\bar{\epsilon}^a_{yy}$) upon the actuation strain e_a is obtained from the finite element (FE) simulations. We proceed to summarize these findings.

2.1. Equi-biaxial loading

Consider the composite lattice of Fig. 1 and assume that the struts of phase A and phase B comprise solids of Young's modulus E_A and E_B, respectively. The second moment of area per unit depth into the page is given by $I_A = t_A^3/12$ for phase A struts and $I_B = t_B^3/12$ for phase B struts. It is shown in Appendix A.1 that the bulk modulus $\bar{K} = \bar{E}_{xx}/2$ is given by

$$\frac{\bar{K}}{E_B \bar{t}_B^3} = \frac{\bar{\sigma}}{2\bar{\epsilon}_{xx} E_B \bar{t}_B^3} = \frac{4\,(1+2r)}{(8+3r)\sin^2\omega} \tag{6}$$

where

$$\bar{t}_B = \frac{t_B}{l}, \tag{7}$$

and

$$r = \frac{E_A I_A}{E_B I_B}. \tag{8}$$

Upon introducing a reference relative density by taking $t_A = 0$ such that

$$\bar{\rho}_{\text{ref}} = \bar{\rho}\cos^2\omega|_{t_A=0} = 2\bar{t}_B \tag{9}$$

the bulk modulus can be re-expressed as

$$\frac{\bar{K}}{E_B \bar{\rho}_{\text{ref}}^3} = \frac{1+2r}{2\,(8+3r)\sin^2\omega}. \tag{10}$$

We note in passing that the overall relative density $\bar{\rho}$ is closely related to $\bar{\rho}_{\rm ref}$ by

$$\bar{\rho} = \frac{(t_A/l) + \rho_{\rm ref}}{\cos^2\omega} \tag{11}$$

upon making use of Eqs. (4) and (9). The bulk modulus decreases with increasing inclination ω and, since we have neglected the contribution to macroscopic compliance from axial stretching of the bars, we find that the bulk modulus is unbounded when $\omega = 0^\circ$. An increased ratio of bending stiffness of the beams of phase A to that of the beams of phase B also increases the macroscopic bulk modulus.

A comparison of finite element predictions with Eq. (10) is given in Fig. 4(a) for the choice $\bar{\rho}_{\rm ref} = 10^{-3}$. In the FE analysis, there were 3 degrees of freedom at each node: a transverse deflection v^h, a rotation θ^h of the cross-section and an axial displacement u^h. Hermitian cubic shape functions were used for interpolation of v^h and θ^h in order to achieve C^1 continuity, whereas linear shape functions were used for u^h. The simulations were performed on a unit cell of size $2l\cos\omega \times 2l\cos\omega$ with periodic boundary conditions, as shown in Fig. A1(c).

As already mentioned above, the finite element calculations reveal that the Poisson ratio $\bar{\nu}_{xy}$ vanishes, and also $\bar{E}_{xx} = \bar{E}_{yy}$. Equi-biaxial stressing on the macroscopic level generates a state of equi-biaxial straining $\bar{\epsilon}_{xx} = \bar{\epsilon}_{yy} = \bar{\epsilon}_v$, with volumetric strain $2\bar{\epsilon}_v$, and the bulk modulus is given by

$$\bar{K}_{\rm FE} = \frac{\bar{\sigma}_{xx} + \bar{\sigma}_{yy}}{4\bar{\epsilon}_v}. \tag{12}$$

The agreement between FE and analysis is excellent over parameter value range of interest.

2.2. Shear loading

The macroscopic shear modulus $\bar{G}_{xy}$ is derived in Appendix A.2. We find that

$$\frac{\bar{G}_{xy}}{E_B\bar{\rho}_{\rm ref}^3} = \frac{2+7r}{4\,(8+3r)\cos^2\omega} \tag{13}$$

where $\bar{\rho}_{\rm ref}$ has already been defined in Eq. (9). FE-based simulations, using periodic boundary conditions, were in excellent agreement to the analytical predictions, see Fig. 4(b).

2.3. Macroscopic Swelling of lattice

The analytical calculations give closed-form expressions for $\bar{K}$ and $\bar{G}_{xy}$. However, no such expressions have been derived for the macroscopic strain $(\bar{\epsilon}^a_{xx},\ \bar{\epsilon}^a_{yy})$ in terms of the linear expansion strain e_a of phase A. FE calculations were used to determine this relationship, as follows.

Start with the simplest case such that $\omega = 0^\circ$ as shown in Fig. 5(a): symmetry dictates that the macroscopic strain vanishes, $\bar{\epsilon}^a_{xx} = \bar{\epsilon}^a_{yy} = 0$. For a lattice of non-vanishing inclination, $\omega \neq 0$, finite element simulations are performed on the unit cell in order to deduce the macroscopic actuation strain due to an imposed actuation strain e_a of phase A. This is done by applying periodic boundary conditions with an imposed actuation strain e_a and vanishing macroscopic strain $\bar{\epsilon}_{ij}$. A macroscopic stress ($\bar{\sigma}_{xx}$, $\bar{\sigma}_{yy}$) is generated, and inversion of the elasticity relation Eq. (5) provides the macroscopic actuation strain, as expressed by:

$$\begin{bmatrix} \bar{\epsilon}^a_{xx} \\ \bar{\epsilon}^a_{yy} \end{bmatrix} = - \begin{bmatrix} 1/\bar{E}_{xx} & 0 \\ 0 & 1/\bar{E}_{xx} \end{bmatrix} \begin{bmatrix} \bar{\sigma}_{xx} \\ \bar{\sigma}_{yy} \end{bmatrix}. \tag{14}$$

Linearity of the kinematics dictates that $\bar{\epsilon}^a_{xx}/e_a$ and $\bar{\epsilon}^a_{yy}/e_a$ are functions of t_A/t_B, ω and $\bar{\rho}_{\text{ref}}$. Finite element predictions of the $\bar{\epsilon}^a_{xx}/e_a$ and $\bar{\epsilon}^a_{yy}/e_a$ versus inclination ω are given in Fig. 5(b) for the choice $\bar{\rho}_{\text{ref}} = 0.1$. Upon swelling of phase A, the lattice shrinks macroscopically, with somewhat greater shrinkage in the x direction than in the y direction. The magnitude of the macroscopic shrinkage in each direction increases with increasing ω, and with increasing thickness of the actuating bar A relative to that of bar B. However, the magnitude of macroscopic strain is independent of relative density[†] and is always less than the actuation strain of phase A by almost an order of magnitude.

2.4. Mechanical maps

Maps to summarise the mechanical properties of the two-phase lattice are shown in Fig. 6. Parts (a) and (b) of Fig. 6 contain maps of bulk and shear modulus maps for $\omega = 1^\circ$ and $\omega = 20^\circ$, respectively. The bulk modulus of the composite lattice decreases with increasing ω, as already noted in connection with the explicit formula Eq. (6). In contrast, the shear modulus is relatively insensitive to the value of ω. We note from Fig. 6(c) that the macroscopic volumetric strain, due to expansion of phase A, ranges from positive to negative values. However, for the example shown of $\omega = 20^\circ$, the lattice undergoes a volumetric shrinkage when the struts of phase A expand for almost the full range of geometries as defined by the axes of the map.

[†]It is assumed that the relative density is sufficiently small for inextensional beam theory to apply for both struts A and B.

2.5. Mechanical failure due to swelling of actuation material

Mechanical failure of the 2-phase lattice can result from macroscopic loading or from swelling of the active material: upon actuation of phase A, the scaffold struts of phase B bend and may fracture. Consider, by way of example, a lattice with $\omega = 0°$, as shown in Fig. 5(a). When all struts of phase A are actuated, the supporting structure B bends. The nodes of structure B remain at their original positions but all rotate by the same angle. The induced axial force P in the actuating bar and moment M_P in the support structure B are calculated as a function of the actuation $e_a l$ as

$$P = \frac{24 E_B I_B}{l^2} e_a, \text{ and} \tag{15}$$

$$M_P = \frac{1}{2} P l = \frac{6 E_B I_B}{l} e_a. \tag{16}$$

The maximum bending stress $\sigma_{\max}$ on the cross-section of bar of phase B can be written in dimensionless form as

$$\frac{\sigma_{\max}}{E_B e_a} = 3 \bar{t}_B. \tag{17}$$

Note the linear dependence of $\sigma_{\max}$ upon $\bar{t}_B$ for the choice $\omega = 0°$.

Now consider the case of a non-vanishing inclination angle ω. As discussed above, an analytical solution is not immediately available for the macroscopic actuation strain and thereby for the induced bending moments in bar of phase B. Finite element simulations are needed to investigate the relationship between bending stress in lattice B and the actuation of the struts A, and this was done as follows. The maximum tensile stress within lattice B was determined for the choices $\omega = 1°$ and $\omega = 20°$, with full constraint of the macroscopic strain, $\bar{\epsilon}_{ij} = 0$. Contours of $\sigma_{\max}/(E_B e_a)$ in the 2D space of $\bar{t}_B$ versus t_A/t_B are given in Fig. 6(d). The induced bending stress again scales almost linearly with the thickness $\bar{t}_B$ of the lattice B. Also, the sensitivity of bending stress to the ratio of bar thicknesses t_A/t_B increases dramatically with increasing ω. The kink in the contour plot for $\omega = 20°$ is due to a change in the location of failure within the lattice: for small t_A/t_B the maximum bending stress is more likely to occur at the obtuse angle of the diamond, while for large t_A/t_B the maximum bending stress will more likely take place at the acute angle.

3. Electrical performance of the solid-state battery

3.1. 1D battery model

The battery under investigation is sketched in Fig. 7(a). It consists of a lithium metal anode, a solid-electrolyte thin layer as the separator, a composite cathode and a current collector. We shall develop a 1D model for the discharge characteristic of a solid-state Li-ion battery containing the microarchitured composite cathode as shown in Fig. 7(b). Our analysis builds on the methodology of McMeeking and co-workers (Mykhaylov et al., 2019) for a Li-ion battery with a composite cathode, as shown in Fig. 7(a). First, we consider the case of a conventional composite cathode, and we then modify the analysis to deal with the micro-architectured cathode based on the microstructure analysed above.

Attention is restricted to a 1D model such that all variations are with respect to an X coordinate, as defined in Fig. 7(a), with origin at the interface between the Li anode and the separator. The separator (in the form of thin layer of electrolyte) and composite cathode are of thickness w and W, respectively. During discharge, lithium ions migrate from lithium metal, through the separator and into active particles of the composite cathode. The filling of cathode particles is spatially non-uniform in X, and occurs within a transition zone of length λ. As filling proceeds, the transition zone advances into unfilled cathode material and leaves in its wake filled cathode of thickness W_f. Three parameters dictate the rate of lithium transport: the lithium concentration $C(X,t)$, ionic electrostatic potential in the solid electrolyte $\phi(X,t)$ and electronic potential in the storage material $\phi_s(X,t)$. We assume that the electrolyte and filled composite cathode are electronic insulators, hence $\phi_s(X,t)$ is constant in the filled portion of the cathode where the electron current vanishes. The cell potential ϕ_{cell} equals the potential difference between the electrodes, such that

$$\phi_{\text{cell}} = \phi_s(w+W,t) - \phi(0^-,t), \tag{18}$$

where $\phi(0^-,t)$ is the potential of the lithium metal over $X < 0$. We proceed to state the potentials in different parts of the cell under galvanostatic discharge at a current density i.

1. In the lithium metal ($X < 0$). Assume that the lithium metal is a perfect conductor with an electric potential set to zero,

$$\phi(0^-,t) = 0. \tag{19}$$

2. At the Li|Separator interface ($X = 0$). Assume a linearized Butler–Volmer reaction at this interface. Define i_0^a as the exchange current at the anode side, and α_{aa} and α_{ac} as symmetric coefficients at the anode|separator interface. Denote the Faraday constant by F, the Universal gas constant by R and the absolute temperature by T in the usual manner. Then, the current across the interface is

$$i = i_0^a \left(\frac{\alpha_{aa} F \eta_a}{RT} + \frac{\alpha_{ac} F \eta_a}{RT} \right) \tag{20}$$

where the overpotential η_a reads

$$\eta_a = \phi(0^-, t) - \phi(0^+, t) - U_a, \tag{21}$$

and U_a is the open-circuit equilibrium potential across the Li|Separator. Now write the interfacial resistance as

$$Z_a = \frac{RT}{i_0^a F(\alpha_{aa} + \alpha_{ac})}, \tag{22}$$

such that Eq. (20) can be rewritten as

$$\eta_a = i Z_a. \tag{23}$$

Taking into account Eq. (19), the value of ϕ at $X = 0^+$ in the separator is

$$\phi(0^+, t) = -U_a - i Z_a. \tag{24}$$

3. In the separator ($0 < X < w$). Assume that Ohm's law governs the Li^+ transport, such that

$$i = -\chi \frac{\partial \phi}{\partial X} \tag{25}$$

where χ is the ionic conductivity of the separator. Integration of Eq. (25) gives immediately

$$\phi(X, t) = \phi(0^+, t) - \frac{i}{\chi} X = -U_a - i Z_a - \frac{i}{\chi} X. \tag{26}$$

such that

$$\phi(w, t) = -U_a - i Z_a - \frac{iw}{\chi}. \tag{27}$$

4. In the composite cathode: filled region ($w < X < w + W_f$). Ohm's law is again assumed in this region, to give

$$i = -\chi_c \frac{\partial \phi}{\partial X} \tag{28}$$

where χ_c is the ionic conductivity of the composite cathode. The potential in this region is thus expressed as

$$\phi(X,t) = -U_a - iZ_a - \frac{iw}{\chi} - \frac{i}{\chi_c}(X-w). \tag{29}$$

and, at $X = w + W_f$, we obtain

$$\phi(w+W_f,t) = -U_a - iZ_a - \frac{iw}{\chi} - \frac{iW_f}{\chi_c}. \tag{30}$$

5. In the composite cathode: unfilled region ($w + W_f < X < w + W$). The current i in the external circuit is the sum of the ionic current in the electrolyte $i_{\mathrm{Li^+}}$ and the electronic current in the active cathode material $i_{\mathrm{e^-}}$. The ionic conductivity χ_c of solid electrolyte is taken to be the same as that in the filled region and the electronic conductivity of active material is χ_e. Consequently,

$$i = i_{\mathrm{Li^+}} + i_{\mathrm{e^-}} \tag{31}$$

where

$$i_{\mathrm{Li^+}} = -\chi_c \frac{\partial \phi}{\partial X}, \text{ and} \tag{32}$$

$$i_{\mathrm{e^-}} = \chi_e \frac{\partial \phi_s}{\partial X}. \tag{33}$$

Charge neutrality demands that the ionic flux into unfilled storage particles equals the electron flux into these particles. Consequently, $\partial i_{\mathrm{Li^+}}/\partial X$ equals $\partial i_{\mathrm{e^-}}/\partial X$. Since i is constant, integration of Eq. (31) from $w + W_f$ to X yields

$$\phi_s(X,t) = \phi_s(w+W_f,t) + \frac{\chi_c}{\chi_e}\phi(w+W_f,t) - \frac{\chi_c}{\chi_e}\phi(X,t) - \frac{i(X-w-W_f)}{\chi_e} \tag{34}$$

Now assume a linearized Butler–Volmer-type reaction at the electrolyte|active particle interface. Define a as the interface area per unit volume of the composite cathode, α_{ca} and α_{cc} as symmetric coefficients at the electrolyte|cathode particle interface, i_0^a as the exchange current at anode side. Then

$$\frac{\partial i_{\mathrm{Li^+}}}{\partial X} = -a i_0^c \left(\frac{\alpha_{ca} F \eta_c}{RT} + \frac{\alpha_{cc} F \eta_c}{RT} \right), \tag{35}$$

where the overpotential is

$$\eta_c = \phi_s(X,t) - \phi(X,t) - U_c. \tag{36}$$

Now define

$$Z_c = \frac{RT}{i_0^c F(\alpha_{ca} + \alpha_{cc})}. \tag{37}$$

Then, upon combining Eqs. (32) and (35), and making use of Eq. (34) a second-order linear differential equation of ϕ is obtained, of the form

$$\frac{\partial^2 \phi}{\partial X^2} + \frac{a\,(\chi_c + \chi_e)}{Z_c \chi_c \chi_e}\phi = \frac{a}{Z_c \chi_c}\left[\phi_s(w + W_f, t) + \frac{\chi_c}{\chi_e}\phi(w + W_f, t) - \frac{i(X - w - W_f)}{\chi_e} - U_c\right] \tag{38}$$

At the filled|unfilled interface ($X = w + W_f$), Li^+ is the only charge carrier. In contrast, the cathode|current collector interface ($X = w + W$) is impermeable to Li^+, thus e^- is the only charge carrier. Hence, the boundary conditions for solution of Eq. (38) are

$$\frac{\partial \phi}{\partial X}(w + W_f, t) = -\frac{i}{\chi_c}, \text{ and} \tag{39}$$

$$\frac{\partial \phi}{\partial X}(w + W, t) = 0. \tag{40}$$

The complementary function ϕ_C in the solution of Eq. (38) can be written as

$$\phi_C(X,t) = A_1 \cosh\frac{X}{\lambda} + A_2 \sinh\frac{X}{\lambda} \tag{41}$$

while a particular integral ϕ_P is

$$\phi_P(X,t) = \frac{\chi_e}{\chi_e + \chi_c}\left[\phi_s(w + W_f, t) + \frac{\chi_c}{\chi_e}\phi(w + W_f, t) - \frac{i(X - w - W_f)}{\chi_e} - U_c\right] \tag{42}$$

where

$$\lambda = \sqrt{\frac{Z_c \chi_e \chi_c}{a(\chi_e + \chi_c)}}. \tag{43}$$

Upon defining λ_0 as

$$\lambda_0 = \sqrt{\frac{Z_c \chi_c}{a}}, \tag{44}$$

λ is then expressed as

$$\lambda = \frac{\lambda_0}{\sqrt{\chi_c/\chi_e + 1}}. \tag{45}$$

Thus, the general solution $\phi = \phi_C + \phi_P$ in the unfilled region is

$$\phi(X,t) = A_1 \cosh\frac{X}{\lambda} + A_2 \sinh\frac{X}{\lambda} + \frac{\chi_e}{\chi_e+\chi_c}\left[\phi_s(w+W_f,t) + \frac{\chi_c}{\chi_e}\phi(w+W_f,t) - \frac{i(X-w-W_f)}{\chi_e} - U_c\right]. \tag{46}$$

Now make use of boundary conditions Eqs. (39) and (40) to eliminate A_1 and A_2, using Eq. (30) to obtain

$$\begin{aligned}\phi(X,t) =& -U_a - iZ_a - \frac{iw}{\chi} - \frac{iW_f}{\chi_c} - \frac{i(X-w-W_f)}{\chi_e+\chi_c} \\ &+ \frac{i\lambda}{(\chi_e+\chi_c)\sinh\frac{W-W_f}{\lambda}}\left(\cosh\frac{X-w-W_f}{\lambda} + \frac{\chi_e}{\chi_c}\cosh\frac{X-w-W}{\lambda}\right. \\ &\left. -1 - \frac{\chi_e}{\chi_c}\cosh\frac{W-W_f}{\lambda}\right).\end{aligned} \tag{47}$$

Likewise, ϕ_s is obtained by substituting Eq. (47) into Eq. (34) to get

$$\begin{aligned}\phi_s(X,t) =& U_c - U_a - iZ_a - \frac{iw}{\chi} - \frac{iW_f}{\chi_c} - \frac{i(X-w-W_f)}{\chi_e+\chi_c} \\ &- \frac{i\lambda}{(\chi_e+\chi_c)\sinh\frac{W-W_f}{\lambda}}\left(\frac{\chi_c}{\chi_e}\cosh\frac{X-w-W_f}{\lambda} + \cosh\frac{X-w-W}{\lambda}\right. \\ &\left. +1 + \frac{\chi_e}{\chi_c}\cosh\frac{W-W_f}{\lambda}\right)\end{aligned} \tag{48}$$

It is convenient to introduce the normalized values

$$\bar{X} = \frac{X-w-W_f}{\lambda}, \qquad \bar{W} = \frac{W-W_f}{\lambda}, \qquad \bar{\chi}_c = \frac{\chi_c}{\chi_e}, \tag{49}$$

such that the current carried by Li-ion can be expressed as

$$\frac{i_{\mathrm{Li}^+}}{i} = \frac{\bar{\chi}_c}{1+\bar{\chi}_c} - \frac{\bar{\chi}_c}{(1+\bar{\chi}_c)\sinh\bar{W}}\left[\sinh\bar{X} + \frac{1}{\bar{\chi}_c}\sinh\left(\bar{X}-\bar{W}\right)\right]. \tag{50}$$

The ionic conductivity of solid electrolyte is typically on the order of $10^{-3}\,\mathrm{S\,cm^{-1}}$, as listed in Table 1. We take $\chi = 2\times10^{-3}\,\mathrm{S\,cm^{-1}}$ for the pure solid electrolyte and $\chi_c = 2\times10^{-4}\,\mathrm{S\,cm^{-1}}$ for the composite cathode. As for the electronic conductivity χ_e, as shown in Table 2, cathode materials have poor electronic conductivity ($10^{-4}\,\mathrm{S\,cm^{-1}}$ or lower), but the addition of conductive agents (such as graphite powder) will greatly increase the electronic conductivity of the composite cathode. The currents $\mathrm{Li^+}$ and $\mathrm{e^-}$ are plotted in Fig. 7(c) for the choice

$\chi_c/\chi_e = 0.1$. It shows that lithium insertion is confined to a small region. In this calculation, we have taken the dimensions of the battery cell to be $w = 10\,\mu\text{m}$ and $W = 100\,\mu\text{m}$. The characteristic length scale is $\lambda_0 = 1\,\mu\text{m}$. The imposed constant current density i is set at $2\,\text{mA}\,\text{cm}^{-2}$.

If we take $Z_a = 30\,\Omega\text{cm}^2$, $U_a = 1.2\,\text{V}$ and $U_c = 4.4\,\text{V}$, together with the values of other parameters given earlier in this section, we can plot the potential distributions shown in Fig. 7(d). Now proceed to obtain the internal resistance of the battery cell. The cell potential is the potential difference of ϕ_s at two ends

$$\phi_{\text{cell}} = U_c - U_a - iZ_a - \frac{iw}{\chi} - \frac{iW_f}{\chi_c} - \frac{i(W-W_f)}{\chi_e+\chi_c} - \frac{i\lambda}{(\chi_e+\chi_c)\sinh\frac{W-W_f}{\lambda}}\left[2+\left(\frac{\chi_e}{\chi_c}+\frac{\chi_c}{\chi_e}\right)\cosh\frac{W-W_f}{\lambda}\right]. \tag{51}$$

Now re-write the cell potential in the form

$$\phi_{\text{cell}} = U_c - U_a - iR_{\text{int}}. \tag{52}$$

where R_{int} is the internal resistance of the cell. Then, upon comparing Eq. (51) and Eq. (52) we obtain

$$R_{\text{int}} = Z_a + \frac{w}{\chi} + \frac{W_f}{\chi_c} + \frac{W-W_f}{\chi_e+\chi_c} + \frac{\lambda}{(\chi_e+\chi_c)\sinh\frac{W-W_f}{\lambda}}\left[2+\left(\frac{\chi_e}{\chi_c}+\frac{\chi_c}{\chi_e}\right)\cosh\frac{W-W_f}{\lambda}\right]. \tag{53}$$

In Eq. (53), the width of filled region W_f is time-dependent. During galvanostatic discharge (that is, at constant current), W_f increases at a constant rate such that

$$W_f(t) = \frac{t}{T}W = \frac{it}{Q}W \tag{54}$$

where Q is the coulombic capacity of the cathode, and T is the total time to fill the cathode with Li^+. The addition of conductive agents alters the ratio χ_c/χ_e while keeping χ_c constant: an increase in the electronic conductivity reduces the internal resistance of the battery cell, but the improvement is minor when $\chi_c/\chi_e < 0.1$.

For extreme cases as $0 < \chi_c/\chi_e << 1$ and $0 < \lambda/w << 1$, the internal resistance can be simplified to

$$R_{\text{int}} = Z_a + \frac{w}{\chi} + \frac{W_f}{\chi_c} + \frac{\lambda}{\chi_c}. \tag{55}$$

The four terms represent resistances at the anode|separator interface, in the separator, in the filled region of composite cathode and inside the filling region of the cathode. There is no

contribution to internal resistance from the unfilled region, as the electronic resistance is negligible. The output power is

$$P = i\phi_{\text{cell}}. \tag{56}$$

3.2. Application of the model to the micro-architectured composite cathode

In this section, we consider the cathode design shown in Fig. 7(b), where the cathode has a micro-architectured structure. The solid electrolyte provides both the scaffold and ionic pathways for phase B material of the composite cathode, and active storage material is embedded inside the scaffold as phase A. Similar to the conventional design, lithium ions fill the composite cathode progressively one row of cell at a time, with the f-th row being filled at the current time in Fig. 7(b). As for the conventional cathode of Fig. 7(a), lithium ions are the only charge carrier within the separator and filled region of cathode material; within the unfilled region of cathode, electrons are the only charge carrier; and, within the narrow region, where lithium ions are inserted into the active particles, current is carried by both Li-ions and electrons. The corresponding electrostatic potential in the ion-conducting pathway ϕ and in the electron-conducting pathway ϕ_s are depicted in Fig. 7(d).

We emphasise that cathode storage material is constrained within the composite mixture of phase A and the solid electrolyte support framework is phase B. The corresponding volume fractions are expressed in Eqs. (1) to (3). Denote the volume fraction of active material within phase A by f_{AM}^0; the volume fraction of binder, electronic conductor and electrolyte within phase A is $(1 - f_{AM}^0)$. The active material volume fraction f_{AM} within the composite cathode is

$$f_{AM} = f_A f_{AM}^0. \tag{57}$$

The effective internal resistance of the composite cathode structure would require detailed numerical simulation to account for the actual Li^+ pathways. A simpler calculation of the internal resistance suffices for our purposes by considering a simplified version as sketched in Fig. 8(a). The solid electrolyte scaffold (phase B) is straightened and aligned with the active storage material (phase A). This simplified geometry is slightly less tortuous than the actual structure and thereby possesses a slightly smaller internal resistance, but the discrepancy is within a reasonable tolerance for the broad assessment of the present study. An analytical

treatment of this replacement structure is straightforward, and this structure thereby serves as a good starting point for the estimation of internal resistance.

Assume that, at any time t, lithium fills up to the f-th row of the structure, as shown in Fig. 7(b). Divide the cathode into three parts: filled cells ($0 < X < W_f^{(f-1)}$), a filling row of cells ($W_f^{(f-1)} < X < W_f^{(f)}$) and unfilled cells ($W_f^{(f)} < X < W$).

The distance of a k-th cell from the separator $W_f^{(k)}$ is

$$W_f^{(k)} = k(l + t_B) = \frac{kW^{\mathrm{H}}}{n} \tag{58}$$

where W^{H} is the total width and n is the total number of unit cells in the direction X in the micro-architectured structure. Denote the total coulombic capacity as Q and applied current density as i. Then the total discharge time T

$$T = \frac{Q}{i}, \tag{59}$$

and the time to fill one row ΔT can be estimated from

$$\Delta T = \frac{T}{n} = \frac{Q}{in}. \tag{60}$$

The f-th row is being filled at time t in the range $(f-1)\Delta T < t < f\Delta T$. During this period, Li-ions migrate in the solid electrolyte scaffold and within the filled region ($0 < X < W_f^{(f-1)}$) of the cathode, see Fig. 8(a). We proceed by adopting the model of the previous section for the filling of each cell. Denote the conductivity of the electrolyte scaffold as χ^H and cathode struts as χ_c^H; then, the internal resistance of this micro-architectured structure is

$$R_{\mathrm{int}}^{\mathrm{H}} = Z_a + \frac{w}{\chi} + \frac{W_f^{(f-1)}}{\chi^H + \chi_c^H} + \frac{w_f}{\chi_c^H} + \frac{\lambda}{\chi_c^H} \qquad \text{when} \quad (f-1)\Delta T < t < f\Delta T. \tag{61}$$

Note that at each time step $t = f\Delta T$, the internal resistance is discontinuous. The left- and right-hand limits are expressed as

$$R_{\mathrm{int}}^{\mathrm{H}-}(f\Delta T) = Z_a + \frac{w}{\chi} + \frac{W_f^{(f-1)}}{\chi^H + \chi_c^H} + \frac{l}{\chi_c^H} + \frac{\lambda}{\chi_c^H}, \tag{62}$$

$$R_{\mathrm{int}}^{\mathrm{H}+}(f\Delta T) = Z_a + \frac{w}{\chi} + \frac{W_f^{(f)}}{\chi^H + \chi_c^H} + \frac{\lambda}{\chi_c^H}. \tag{63}$$

In the limit of $n \to \infty$, the internal resistance becomes a linear function of time t

$$R_{\mathrm{int}}^{\mathrm{H}}(t) = Z_a + \frac{w}{\chi} + \frac{W^{\mathrm{H}}}{\chi^H + \chi_c^H}\frac{t}{T} + \frac{\lambda}{\chi_c^H}. \tag{64}$$

As an example, Fig. 8(b) shows the internal resistance of the whole cell for selected values of unit cell n, with the overall length of the cell held fixed. For each unit cell, we take $t_B/l = 0.1$, $t_A/t_B = 5$, and the volume fraction of active material in the composite strut $f^0_{AM} = 0.7$; then, the volume fraction of active material in the structure is $f_{AM} = 0.35$. We note from Fig. 8(b) that, as the length of unit cell is decreased, the internal resistance decreases. The resistance at $n = \infty$ is the lowest achievable value.

It is instructive to compare the electrical performance of this micro-architectured cathode with that of the conventional composite cathode as detailed in the previous section. Assume that the micro-architectured cathode can achieve the same coulombic capacity Q, and discharges at the same current density i, as the conventional cathode. Then, we can compare the resistance evolution of the two cathodes during lithiation. The same coulombic capacity indicates that the content of active materials will be the same for the micro-architectured structure and the conventional cathode. Consequently,

$$f^0_{AM} W = W^{\mathrm{H}} f_{AM} \tag{65}$$

if we assume the height and thickness of the two structures to be the same. Upon recalling Eq. (57), we obtain a relation between the two widths,

$$W = f_A W^{\mathrm{H}}. \tag{66}$$

Then, according to Eq. (59), the total discharge time will be the same for the two structures. Since both solid electrolyte and cathode struts in the micro-architectured design are straight, their conductivities can be expressed as

$$\chi^H = \chi f_B, \quad \chi_c^H = \chi_c f_A. \tag{67}$$

A representative time $t = T/2$ is chosen for the time at which a comparison is made of the resistance of the two structures. The resulting relative resistance is

$$R^{\mathrm{rel}}_{\mathrm{int}} = \frac{R^{\mathrm{H}}_{\mathrm{int}}(T/2)}{R_{\mathrm{int}}(T/2)} = \frac{Z_a + w\chi^{-1} + W^{\mathrm{H}}\left[2\left(\chi^H + \chi_c^H\right)\right]^{-1} + \lambda\left(\chi_c^H\right)^{-1}}{Z_a + w\chi^{-1} + W\left(2\chi_c\right)^{-1} + \lambda\chi_c^{-1}}, \tag{68}$$

and, upon combining Eqs. (66) to (68), we find

$$R^{\mathrm{rel}}_{\mathrm{int}} = \frac{R^{\mathrm{H}}_{\mathrm{int}}(T/2)}{R_{\mathrm{int}}(T/2)} = \frac{Z_a + w\chi^{-1} + W\left[2f_A\left(\chi f_B + \chi_c f_A\right)\right]^{-1} + \lambda\left(\chi_c f_A\right)^{-1}}{Z_a + w\chi^{-1} + W\left(2\chi_c\right)^{-1} + \lambda\chi_c^{-1}}. \tag{69}$$

The map of relative resistance is shown in Fig. 8(c). In general, the internal resistance of the lattice cathode exceeds that of the composite cathode ($R_{\text{int}}^{\text{rel}} > 1$), especially when both volume fractions of electrolyte and cathode material are small.

3.3. Design map for a micro-architectured composite cathode

It is instructive to construct a design map for the micro-architectured composite cathode by plotting electrical and mechanical performance parameters using axes of $(\bar{t}_B, \bar{t}_A/\bar{t}_B)$. Based on Figs. 3(b), 6(b-d) and 8(c), we construct a design map in Fig. 9 for the choice $\omega = 20^\circ$. The performance of the lattice-cathode can be quantified as a function of $(\bar{t}_B,\ t_A/t_B)$, as sketched in Fig. 9(a). The porosity limit of $f_{air} \to 0$ is included on the map, by making use of Eq. (3). In particular, for the choice $\omega = 20^\circ$, Eq. (3) reduces to

$$1 - \frac{\bar{t}_B}{\cos^2 20^\circ}\left(\frac{t_A}{t_B} + 2\right) = 0. \tag{70}$$

Boundaries of the performance map

We proceed to quantify the performance map in Fig. 9(b) by adding two boundaries, and three sets of contours of performance. Possible operating regimes of the map are thereby identified. We make use of the same axes as in Fig. 9(a), and again take $\omega = 20^\circ$, with $E_A = E_B$.

(i) The lattice-cathode is only viable when the level of stress in beams of phase B are less than an allowable bending strength $\sigma_{\max}$. Assume that the lattice is fully constrained such that the macroscopic strain vanishes. Then, the locus of geometries for which $\sigma_{\max}/(E_B e_a) = 0.6$ is taken from Fig. 6(d) and added to Fig. 9(b). We take this as a failure locus for the beams of phase B.

(ii) A second boundary is identified by recognising that a low value of $\bar{t}_B$ and of t_A/t_B gives an unacceptably high value of internal resistance R_{int}. Take, as a arbitrary value, $R_{\text{int}}^{\text{rel}} = 2$ for this boundary. Then, the boundary locus is obtained directly from Eq. (69) for the choice $Z_a = 30\,\Omega\,\text{cm}^2$, $w = 10\,\mu\text{m}$, $W = 100\,\mu\text{m}$, $\chi = 2 \times 10^{-3}\,\text{S}\,\text{cm}^{-1}$, $\chi_c = 2 \times 10^{-4}\,\text{S}\,\text{cm}^{-1}$, $\lambda = 1\,\mu\text{m}$, and the volume fractions of A and B from Eqs. (1) and (2).

Performance contours on the map

We proceed to add 3 sets of contours for cathode properties: the volume fraction of phase A, the macroscopic volumetric strain associated with lithiation of storage particles within phase A, and the macroscopic bulk modulus $\bar{K}$ of the lattice.

(i) Contours of volume fraction f_A of phase A are shown for $\omega = 20^\circ$ by direct exploitation of Eq. (1), rewritten in the form

$$f_A = \frac{1}{\cos^2 20^\circ} \frac{t_A}{t_B} \bar{t}_B. \tag{71}$$

(ii) The macroscopic volumetric expansion of the composite lattice is shown by contours of $(\bar{\epsilon}_{xx} + \bar{\epsilon}_{yy})/e_a$, where e_a is the linear expansion of phase A associated with lithiation. These contours are obtained by FE calculation.

(iii) Contours of bulk modulus $\bar{K}/E_B$ are added to the map by direct exploitation of Eq. (10).

It is clear from Fig. 9(b) that, to achieve high storage capacity and low electrical resistance, it is desirable for the porosity f_{air} to be minimized and the cathode volume fraction f_A should be maximised. However, this also indicates a potential mechanical failure due to the fracture of solid electrolyte scaffold, as well as an increased stiffness. In contrast, a low macroscopic modulus and small degree of macroscopic swelling is achieved for a small volume fraction of active material. The optimal operating point in the map depends upon the material properties of cathode material and electrolyte, and with overall performance considerations.

The present analysis assumes that fracture of the lattice is dictated by flexure of the struts. The analysis is linear and neglects the possibility of elastic, or elastic-plastic buckling. Bhandakkar and Johnson (2012) have considered the buckling of a perfect hexagonal honeycomb due to lithiation and show that buckling limits the stress level within the lattice; prior to buckling their lattice is stretching-governed under an in-plane equi-biaxial compressive stress, and so strut failure by bending is not a consideration for them. In contrast, the struts of the present topology bend upon lithiation due to the finite inclination angle ω. Consequently, buckling is not relevant to the topology of the present study unless the struts are extremely slender. Such non-linearities are beyond the scope of the present study.

4. Concluding remarks

In this study, a two-phase 2D lattice material is identified that possesses both a high macroscopic compliance and a low macroscopic coefficient of thermal expansion. The effective properties of the lattice are analysed both analytically and by finite element simulation. The potential of this lattice structure for use as the cathode of solid-state Li-ion battery is explored. To do so, the phase A contains active storage material whereas phase B comprises the solid electrolyte. Thus, the 2-phase structure can alleviate the stresses induced by swelling of the cathode storage material. The targeted active materials are those with extremely high energy density and power density, but currently cannot be used as electrode material because of a high lithiation strain and low mechanical strength. We present a design map that illustrates the competition between mechanical failure and cathode performance, and serves as a tool to aid the optimal topological design of composite cathodes. The 2D lattice of the present study can be considered to be a prismatic lattice in 3 dimensions. Fully 3D lattices ca also be invented but it will be a major challenge to manufacture them.

Acknowledgement

This work was supported by the ERC project 'Multilat' and by the Faraday Institution Solbat and FutureCat (grant number FIRG007 and FIRG017, respectively). Y.Z. is now supported by Shanghai Sailing Program (Project No. 20YF1452300) and the Fundamental Research Funds for the Central Universities.

List of Figures

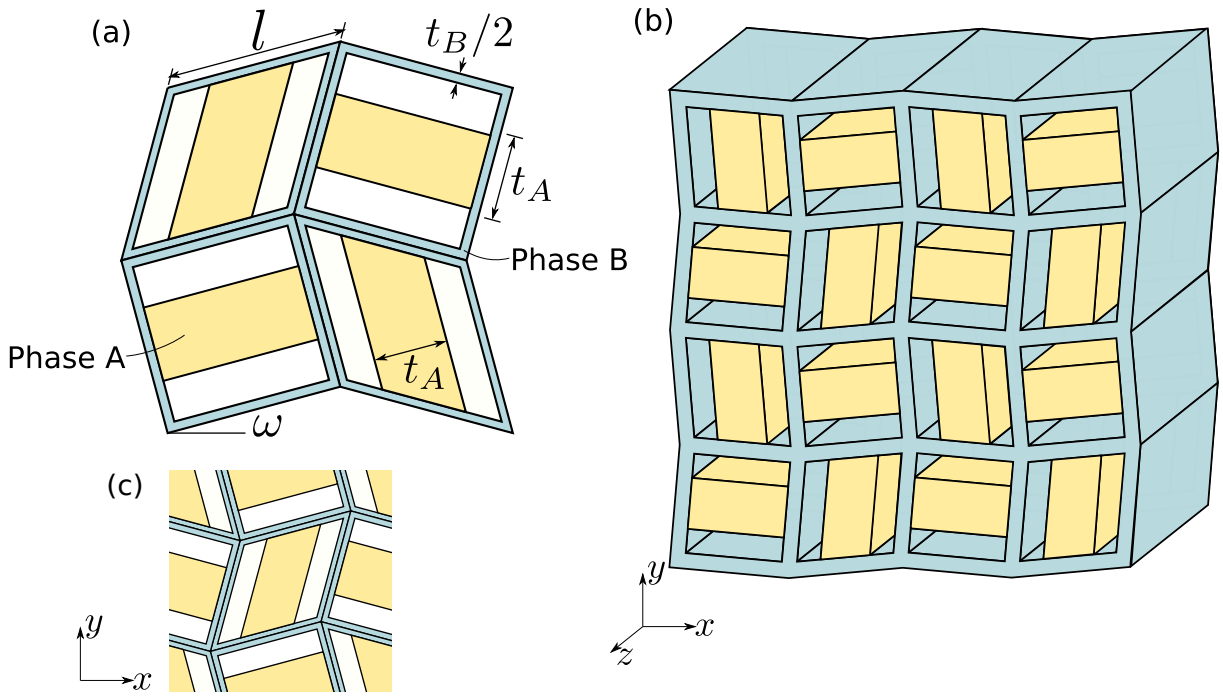

Figure 1: The geometry of two-phase lattice structure. (a) Leading dimensions of a representative 2D unit cell. (b) The 3D structure. (c) The unit cell for numerical calculation. The two phases are identified as phase A and phase B, with dissimilar thermal and mechanical properties. The empty phase of air is uncoloured.

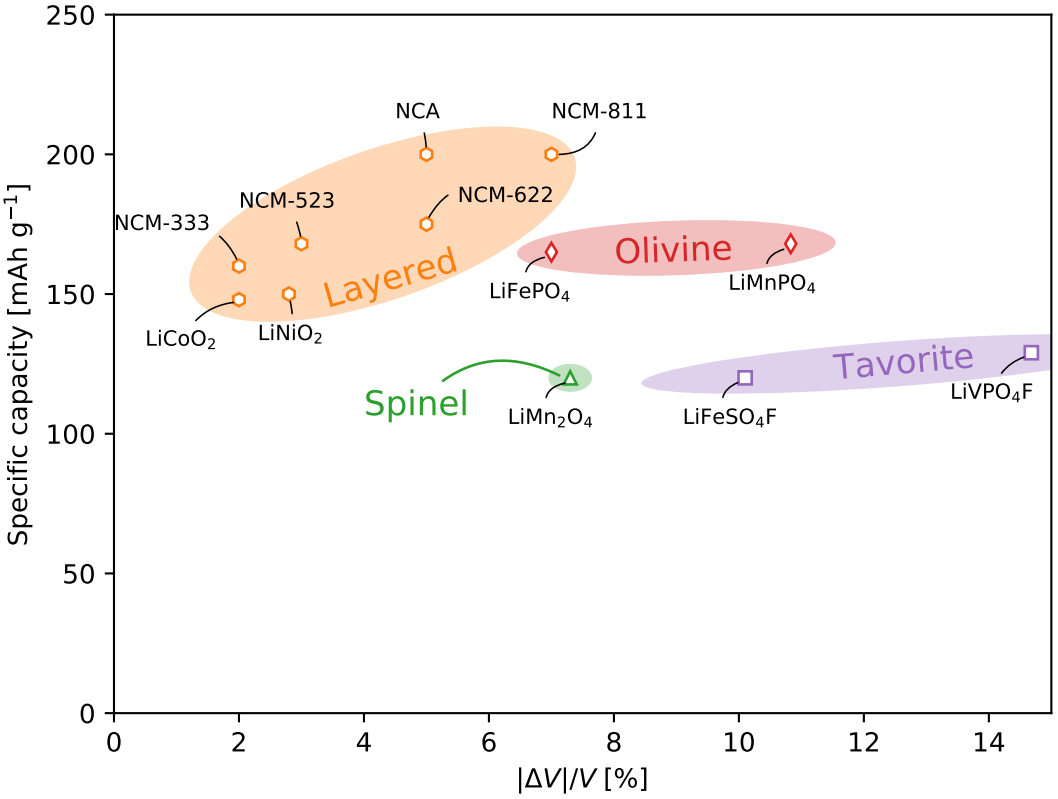

Figure 2: Measured capacity versus volume change upon full lithiation of some typical cathode materials. (Refs: Koerver et al. (2018); Koyama et al. (2006); Nitta et al. (2015); Woodford et al. (2012). NCM-333: $LiNi_{1/3}Co_{1/3}Mn_{1/3}O_2$, NCM-523: $LiNi_{0.5}Co_{0.2}Mn_{0.3}O_2$, NCM-622: $LiNi_{0.6}Co_{0.2}Mn_{0.2}O_2$, NCM-811: $LiNi_{0.8}Co_{0.1}Mn_{0.1}O_2$, NCA: $LiNi_{0.8}Co_{0.15}Al_{0.05}O_2$.)

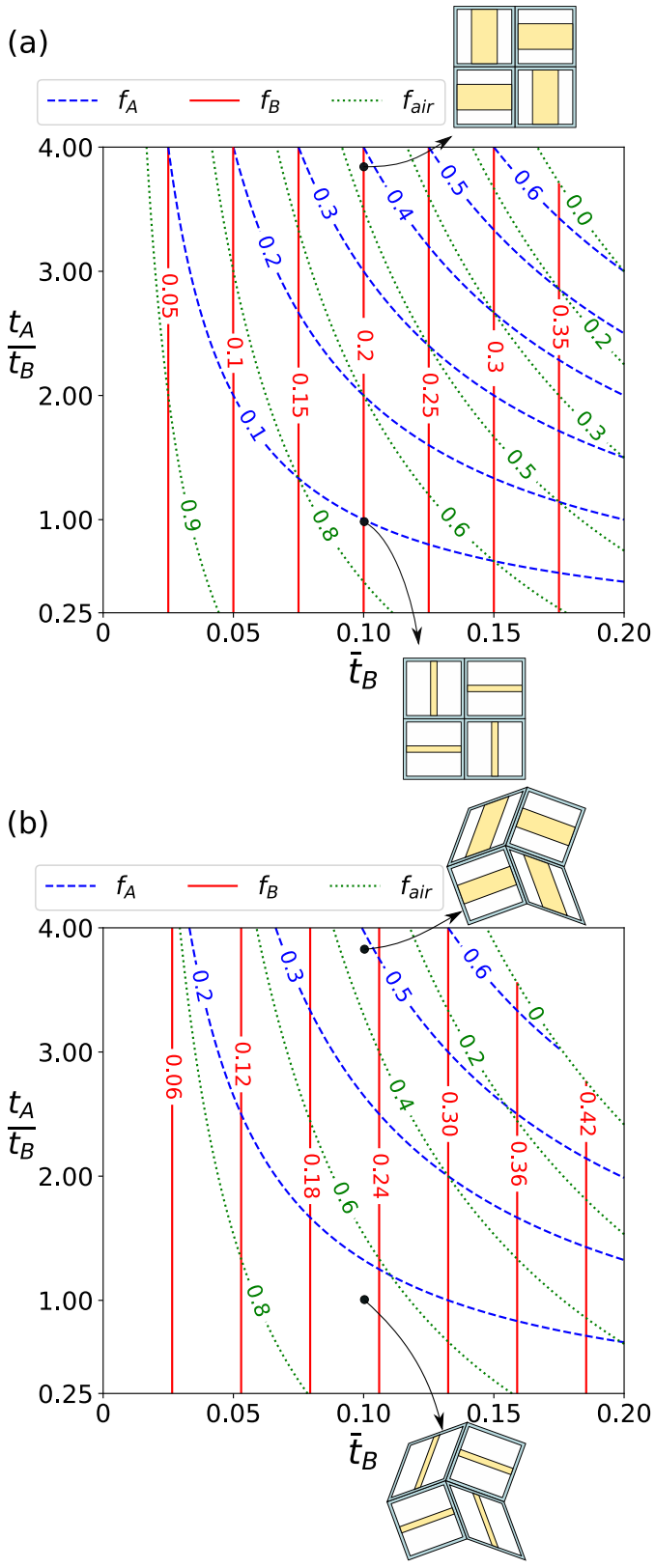

Figure 3: Geometry of (a) $\omega = 0°$ and (b) $\omega = 20°$ composite cathodes, where $\bar{t}_B = t_B/l$. The maps show contours of volume fraction f_A of phase A, f_B of phase B and porosity f_{air}.

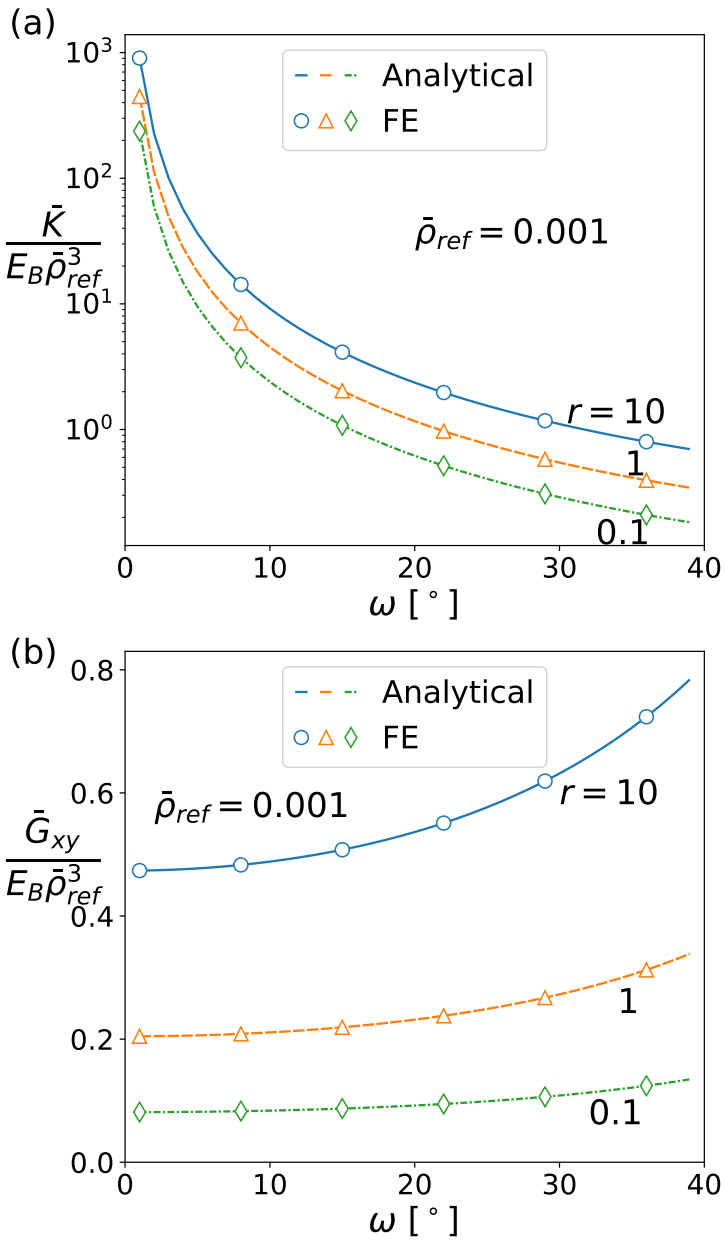

Figure 4: Comparison of FE solution with analytical solution, for $\bar{\rho}_{\mathrm{ref}} = 10^{-3}$ and selected values of the ratio r of the bending stiffnesses of phases A and B. (a) Bulk modulus. (b) Shear modulus.

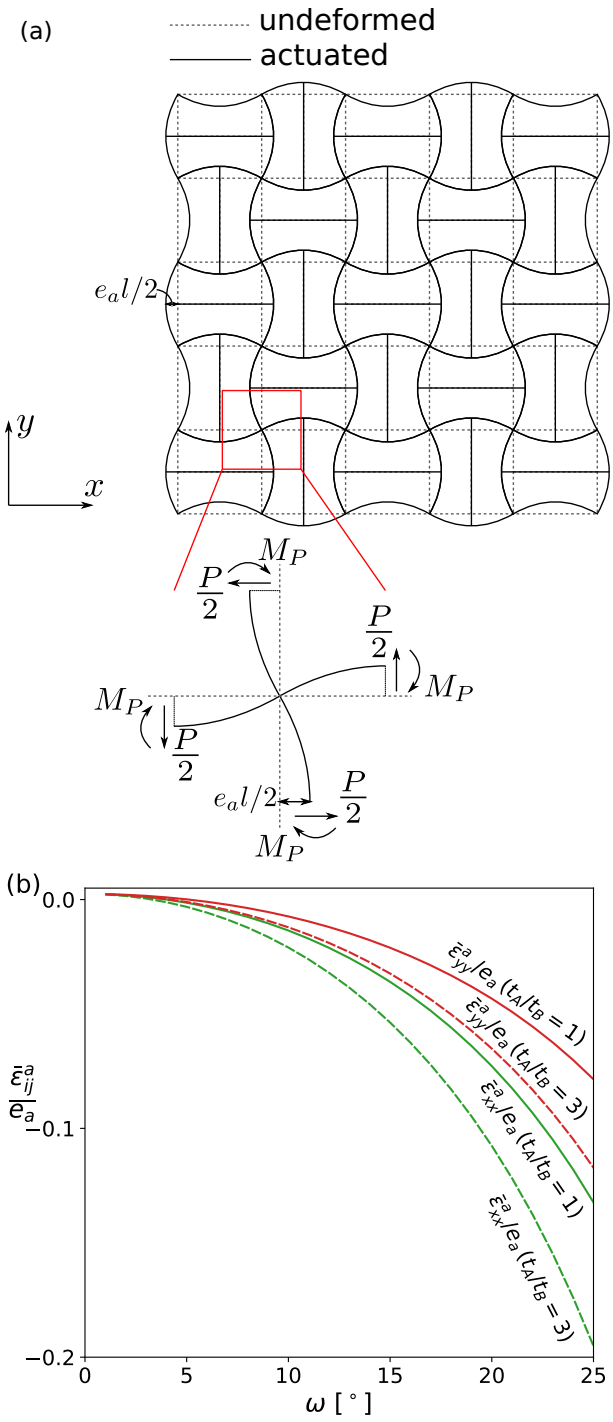

Figure 5: (a) Lattice deformation due to actuation of phase A material with an actuation strain e_a for $\omega = 0°$. (b) Macroscopic actuation strain versus inclination. It shows that when $\omega \neq 0$, the lattice shrinks upon swelling of phase A material, and the shrinkage is slightly greater in the x direction than in the y direction.

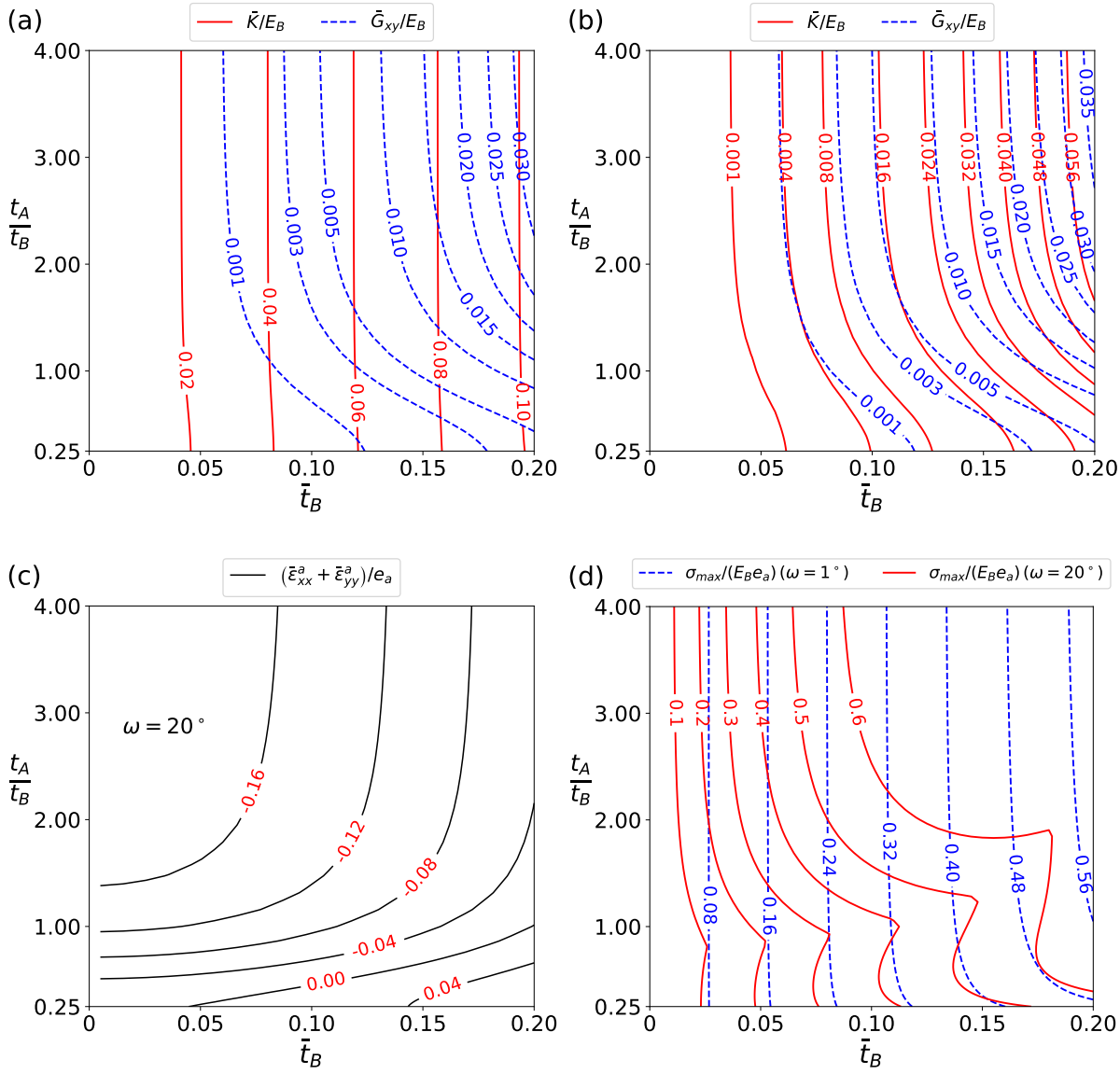

Figure 6: Mechanical maps. Macroscopic bulk and shear moduli for (a) $\omega = 1°$ and (b) $\omega = 20°$. Although the inclination angle ω has great influence on the bulk modulus, it has little influence on the shear modulus. (c) Normalized macroscopic volumetric strain $(\bar{\epsilon}^a_{xx} + \bar{\epsilon}^a_{yy})/e_a$ for a $\omega = 20°$ lattice. By adjusting the thicknesses of strut A and B, the structure can achieve positive, negative and zero thermal expansion coefficient. (d) Normalized maximum local struts $\sigma_{\max}/(E_B e_a)$ for $\omega = 1°$ and $\omega = 20°$ lattices.

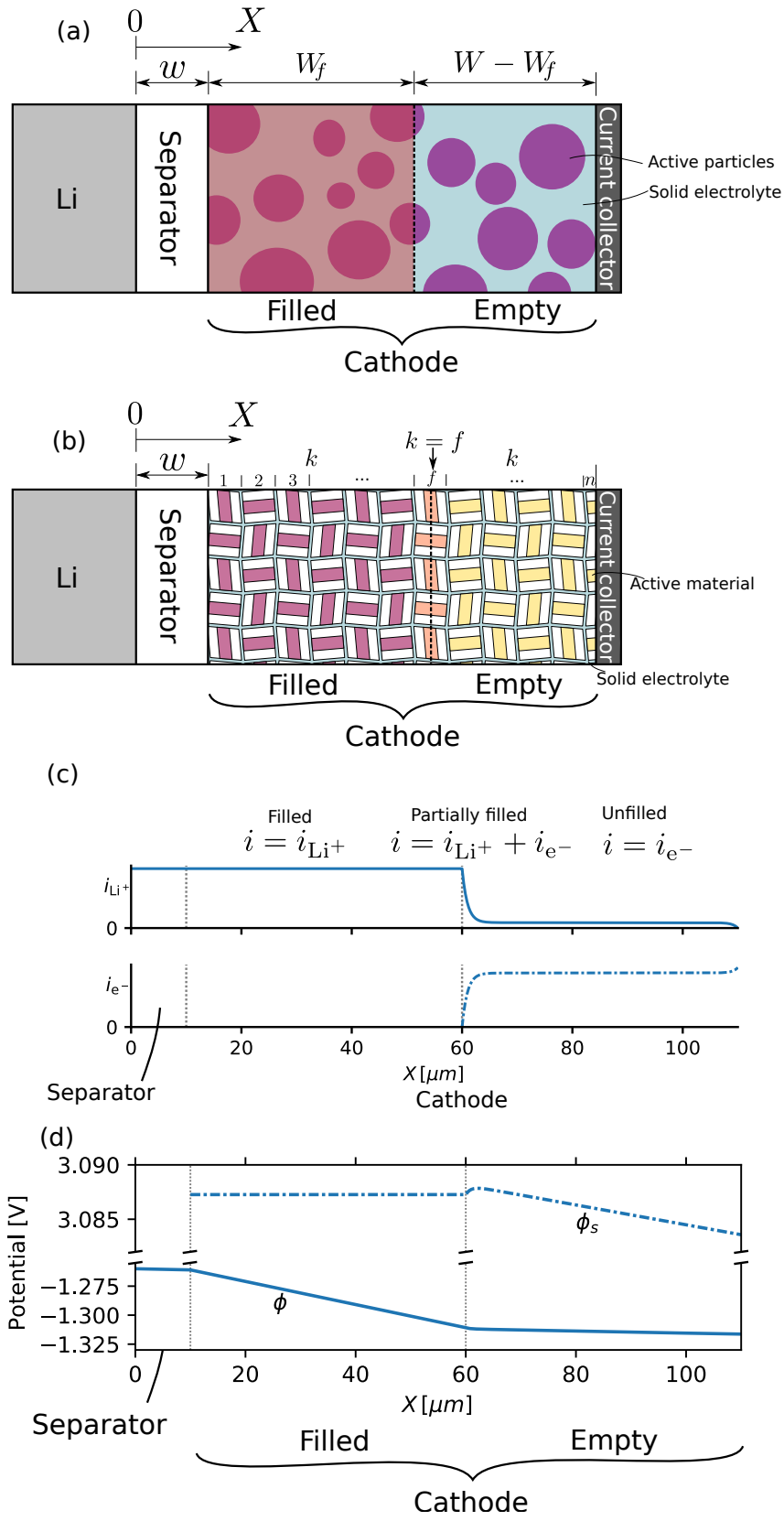

Figure 7: Sketch of a battery cell with (a) composite cathode and (b) micro-architectured cathode. (c) Schematic of the ionic and electron currents in the battery and (d) electric potential.

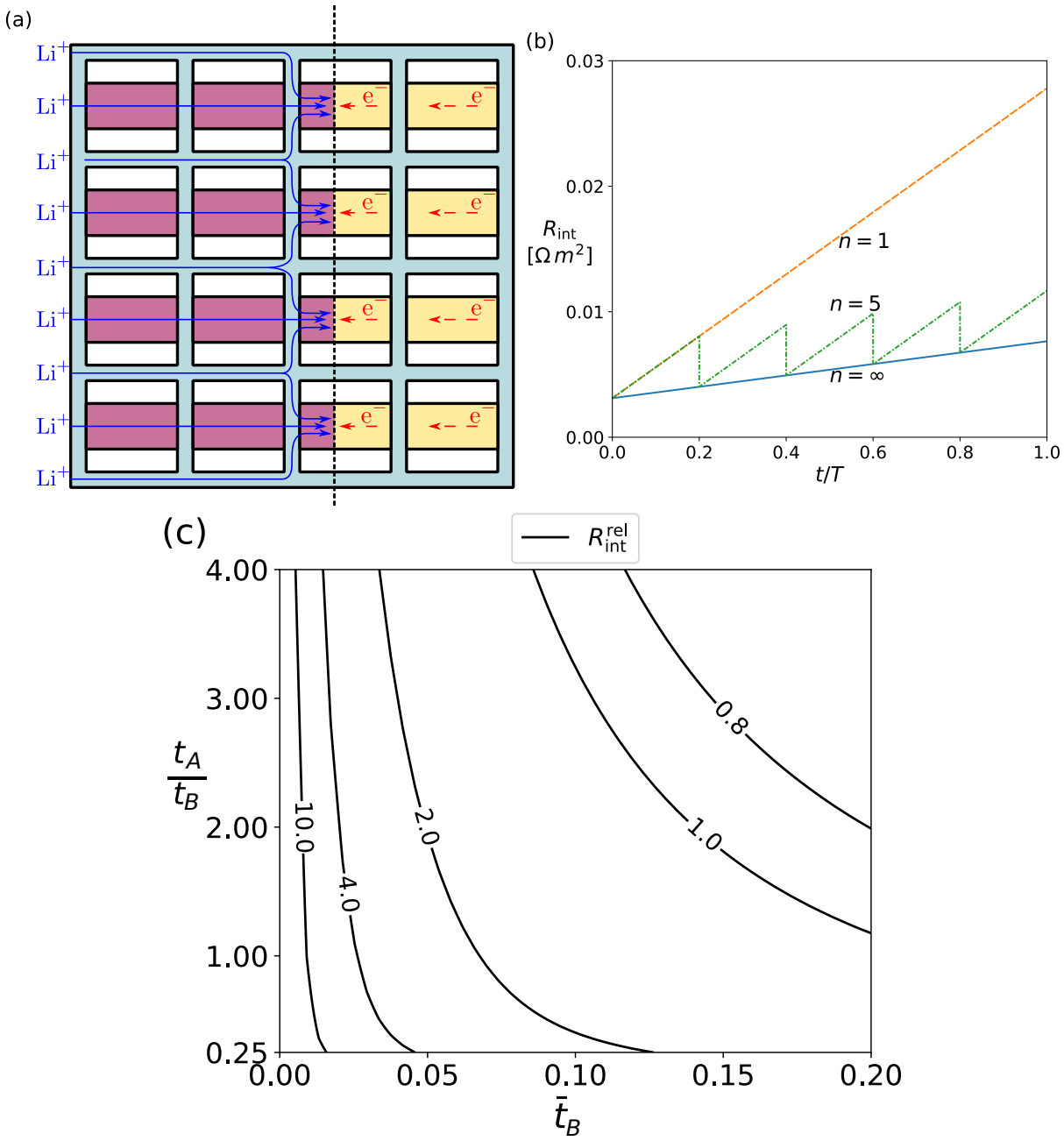

Figure 8: (a) Idealised geometry for the calculation of resistance of the micro-architectured cathode. (b) Internal resistance versus time for cathodes with n layers ($\bar{t}_A = 0.5$, $\bar{t}_B = 0.1$). (c) Internal resistance of the micro-architectured cathode relative to the traditional composite cathode ($n = \infty$).

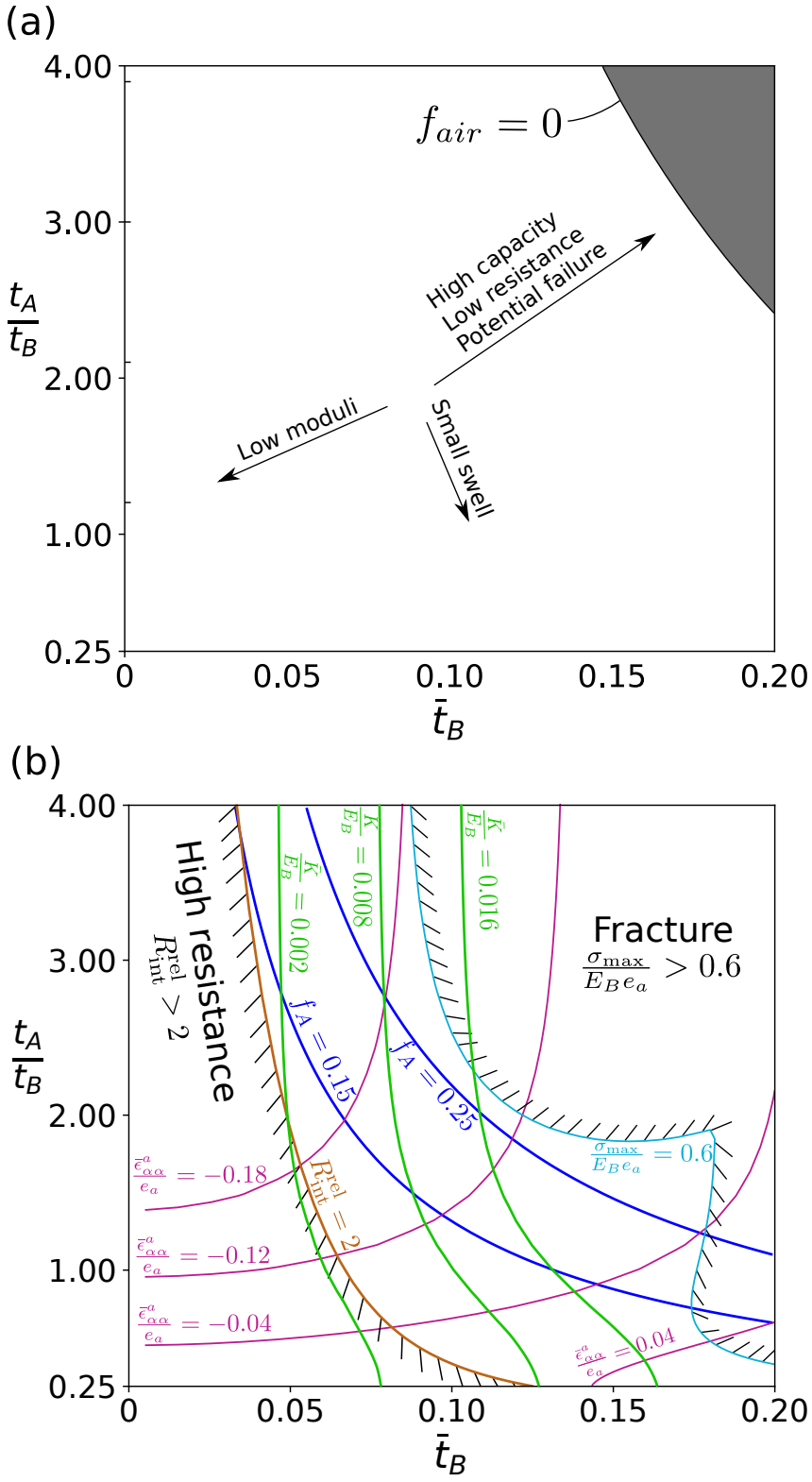

Figure 9: (a) The regimes of performance of the micro-architectured cathode and (b) a design map for a $\omega = 20°$ cathode. Here, $\bar{\epsilon}^a_{\alpha\alpha} = \bar{\epsilon}^a_{xx} + \bar{\epsilon}^a_{yy}$ is the macroscopic swell strain due to an actuation strain e_a of phase A.

Appendix A. Analysis of macroscopic modulus

Analytical expressions for the macroscopic elastic moduli of the composite lattice are obtained by considering equi-biaxial loading to obtain the bulk modulus $\bar{K}$, and then shear loading to determine the shear modulus $\bar{G}_{xy}$.

Appendix A.1. Equi-biaxial loading

Assume equi-biaxial loading of magnitude ($\bar{\sigma}_{xx} = \bar{\sigma}_{yy} = \bar{\sigma}$, $\bar{\sigma}_{xy} = 0$) in the x-y reference frame. Note that lines passing through the centres of the diamonds are at 45° to the x and y axes in Fig. A1(a). Write these two rotated directions as x' and y'. For later analysis, it is convenient to define a representative unit cell in this rotated co-ordinate system (Fig. A1(b)), containing a complete diamond surrounded by four squares (S_1, S_2, S_3, S_4), shown as shaded in the figure.

Now rotate axes to the new x'- y' coordinate system, as shown in Fig. A2. Rotational symmetry dictates that the moments at the mid points of the beams in the squares/diamonds are zero. Application of rotation symmetry and glide reflection symmetry further reduces the number of unknown forces and moments to (F, M, T, P, W), as shown in Fig. A2(b).

Now apply the method of sections to relate the macroscopic hydrostatic loading to the microscopic force distribution of the struts, compare Fig. A2(a) and (b). Force equilibrium demands:

$$2F + P\left(\cos\left(\frac{\pi}{4}-\omega\right)+\sin\left(\frac{\pi}{4}-\omega\right)\right) + W\left(\cos\left(\frac{\pi}{4}-\omega\right)-\sin\left(\frac{\pi}{4}-\omega\right)\right) = 2\sqrt{2}\bar{\sigma}l\cos\omega \tag{A.1}$$

$$2T + P\left(\cos\left(\frac{\pi}{4}-\omega\right)+\sin\left(\frac{\pi}{4}-\omega\right)\right) + W\left(\cos\left(\frac{\pi}{4}-\omega\right)-\sin\left(\frac{\pi}{4}-\omega\right)\right) = 0 \tag{A.2}$$

Additionally, if we consider only one square S_2, as shown in Fig. A2(c), moment balance about the point P_C demands that

$$-\sqrt{2}Fl\sin\omega - 2M + Wl\cos\omega\cos\omega - Pl\cos\omega\sin\omega = 0 \tag{A.3}$$

Eqs. (A.1) to (A.3) can be solved to give

$$F = -\frac{1}{\sqrt{2}}P\cos\omega - \frac{1}{\sqrt{2}}W\sin\omega + \sqrt{2}\bar{\sigma}l\cos\omega \tag{A.4}$$

$$T = -\frac{1}{\sqrt{2}} P \cos\omega - \frac{1}{\sqrt{2}} W \sin\omega \tag{A.5}$$

$$\frac{M}{l} = \frac{1}{2} W - \bar{\sigma} l \cos\omega \sin\omega \tag{A.6}$$

The remaining unknowns are P and W, and we need to consider compatibility in order to proceed. Due to symmetry, we can consider only one square S_2 as representative of the four squares in Fig. A2(a) . Cut the structure at P_4, P_C and P_2 as shown in Fig. A3. By so-doing, we introduce eight unknown forces/moments in addition to P and W: (T_1, T_2, M_1) at P_4 in Beam P_1P_4, the unknowns (T_5, T_6, M_2) at P_4 in Beam P_3P_4, and the unknowns (T_3, T_4) at P_C. The moment vanishes at P_C due to symmetry, as shown in Fig. A3. Equilibrium provides the following 5 relations:

$$T_3 = 2T_2 - W + \bar{\sigma} l \sin 2\omega \tag{A.7}$$

$$T_4 = 2T_1 + P - 2\bar{\sigma} l \cos^2\omega \tag{A.8}$$

$$T_5 = -T_2 + F \sin\left(\frac{\pi}{4} - \omega\right) - T \cos\left(\frac{\pi}{4} - \omega\right) \tag{A.9}$$

$$T_6 = -T_1 + F \cos\left(\frac{\pi}{4} - \omega\right) + T \sin\left(\frac{\pi}{4} - \omega\right) \tag{A.10}$$

$$M_2 = M_1 - M \tag{A.11}$$

and so five more equations are needed in order to solve for the remaining unknowns (P, W, T_1, T_2, M_1). Symmetry and continuity provide the following 4 relations:

$$\begin{aligned}\theta_{P_1} = \frac{l^2}{E_B I_B} \times \Bigg[& \frac{1}{8}\left(P\cos 2\omega + W \sin 2\omega\right) + \frac{1}{4} W + \frac{1}{2}\left(F \sin\left(\frac{\pi}{4} - \omega\right) + T\cos\left(\frac{\pi}{4} - \omega\right)\right) \\ & - \frac{M}{l} - \frac{1}{2} T_3 - 0 \cdot T_4 - \frac{1}{2} T_1 + T_2 - \frac{M_1}{l} \Bigg] = 0\end{aligned} \tag{A.12}$$

$$\begin{aligned}\theta_{P_3} = \frac{l^2}{E_B I_B} \times \Bigg[& -\frac{1}{4} T_4 + \frac{1}{8} T_3 - T_6 + \frac{1}{2} T_5 + \frac{M_2}{l} + \frac{1}{2}\left(T \sin\left(\frac{\pi}{4} - \omega\right) - F\cos\left(\frac{\pi}{4} - \omega\right)\right) \\ & - \frac{M}{l} - \frac{1}{2}\left(-P\sin 2\omega + W\cos 2\omega\right) + \frac{1}{2}\left(P\cos 2\omega + W \sin 2\omega\right) + \frac{1}{2} W \Bigg] = 0\end{aligned} \tag{A.13}$$

$$\begin{aligned}u_{P_{C1}x''} - u_{P_{C2}x''} = \frac{l^3}{E_B I_B} \times \Bigg[& -\frac{1}{24}\left(P\cos 2\omega + W \sin 2\omega\right) - \frac{1}{16} W \\ & - \frac{1}{12}\left(F \sin\left(\frac{\pi}{4} - \omega\right) + T\cos\left(\frac{\pi}{4} - \omega\right)\right) + 0 \cdot \frac{M}{l} \\ & - \frac{1}{16} T_3 - \left(\frac{5}{24} + \frac{1}{24r}\right) T_4 + \frac{1}{12} T_1 + \frac{3}{16} T_2 - \frac{M_1}{4l} \Bigg] \\ & - \frac{l^3}{E_B I_B} \times \Bigg[\left(\frac{1}{8} + \frac{1}{24r}\right) T_4 - \frac{1}{16} T_3 + \frac{1}{4} T_6 - \frac{3}{16} T_5 - \frac{M_2}{8l}\end{aligned}$$

$$
\begin{aligned}
&- \frac{3}{16}\left(T\sin\left(\frac{\pi}{4}-\omega\right) - F\cos\left(\frac{\pi}{4}-\omega\right)\right) \\
&+ \frac{M}{4l} - \frac{1}{8}\left(-P\sin 2\omega + W\cos 2\omega\right) - \frac{3}{16}\left(P\cos 2\omega + W\sin 2\omega\right) - \frac{1}{4}W\Bigg] = 0
\end{aligned} \tag{A.14}
$$

$$
\begin{aligned}
u_{P_{C1}y''} - u_{P_{C2}y''} = \frac{l^3}{E_B I_B} \times \Bigg[& \frac{1}{16}\left(P\cos 2\omega + W\sin 2\omega\right) + \frac{1}{8}W \\
&+ \frac{1}{4}\left(F\sin\left(\frac{\pi}{4}-\omega\right) + T\cos\left(\frac{\pi}{4}-\omega\right)\right) \\
&- \frac{M}{2l} - \frac{7}{24}T_3 - \frac{1}{16}T_4 - \frac{1}{4}T_1 + \frac{29}{48}T_2 - \frac{5M_1}{8l}\Bigg]
\end{aligned} \tag{A.15}
$$

$$
\begin{aligned}
&- \frac{l^3}{E_B I_B} \times \Bigg[-\frac{1}{16}T_4 + \frac{1}{24}T_3 - \frac{1}{8}T_6 + \frac{5}{48}T_5 + \frac{M_2}{8l} \\
&+ \frac{5}{48}\left(T\sin\left(\frac{\pi}{4}-\omega\right) - F\cos\left(\frac{\pi}{4}-\omega\right)\right) - \frac{M}{8l} \\
&- \frac{1}{16}\left(-P\sin 2\omega + W\cos 2\omega\right) + \frac{5}{48}\left(P\cos 2\omega + W\sin 2\omega\right) + \frac{1}{16}W\Bigg] = 0
\end{aligned} \tag{A.16}
$$

where

$$
r = \frac{E_A I_A}{E_B I_B}. \tag{A.17}
$$

In the above equations we have introduced a third coordinate system x''- y'', which is rotated by $(\pi/4+\omega)$ with respect to x'- y'. Compatibility also demands that, for equi-biaxial loading,

$$
u_{P_{C4}x} - u_{P_{C3}x} = \bar{\epsilon}_{xy} l = 0. \tag{A.18}
$$

where the points P_{C3} and P_{C4} have already been defined in the original coordinate system x-y in Fig. A1(a). Upon rewriting Eq. (A.18) in the x''- y'' system we have

$$
\left(u_{P_{C3}x''} - u_{P_{C4}x''}\right)\sin\omega + \left(u_{P_{C3}y''} - u_{P_{C4}y''}\right)\cos\omega = \frac{l^3}{E_B I_B}\left[A_1 - A_2 + A_3 - A_4\right] \tag{A.19}
$$

where

$$
\begin{aligned}
A_1 = \Bigg[& \left(P\sin 2\omega - W\cos 2\omega\right)\left(\frac{1}{16}\cos 2\omega + \left(\frac{1}{8} + \frac{1}{48r}\sin 4\omega\right)\right) \\
&+ \left(P\cos 2\omega + W\sin 2\omega\right)\left(-\frac{1}{24} - \frac{1}{8}\sin 2\omega - \left(\frac{1}{8} + \frac{1}{24r}\right)\sin^2 2\omega\right) \\
&- \left(\frac{5}{48} + \frac{3}{16}\sin 2\omega\right)\left(F\sin\left(\frac{\pi}{4}-\omega\right) + T\cos\left(\frac{\pi}{4}-\omega\right)\right) \\
&+ \left(\frac{1}{8} + \frac{1}{4}\sin 2\omega\right)\frac{M}{l} + \left(\frac{1}{16} + \frac{1}{8}\sin 2\omega\right)T_3 - \left(\frac{1}{24} + \frac{1}{16}\sin 2\omega\right)T_4 \\
&+ \left(\frac{5}{48} + \frac{3}{16}\sin 2\omega\right)T_1 - \left(\frac{1}{8} + \frac{1}{4}\sin 2\omega\right)T_2
\end{aligned}
$$

$$+\left(\frac{1}{8}+\frac{1}{4}\sin 2\omega\right)\frac{M_1}{l}\Bigg]\sin\omega \tag{A.20}$$

$$\begin{aligned}A_2=\Bigg[&\left(\frac{1}{8}-\frac{1}{8}\sin 2\omega\right)T_4+\left(-\frac{1}{16}+\frac{1}{16}\sin 2\omega\right)T_3+\left(\frac{29}{48}-\frac{11}{16}\sin 2\omega\right)T_6\\&+\left(-\frac{1}{4}+\frac{1}{4}\sin 2\omega\right)T_5+\left(-\frac{5}{8}+\frac{3}{4}\sin 2\omega\right)\frac{M_2}{l}\\&+\left(-\frac{1}{4}+\frac{1}{4}\sin 2\omega\right)\left(T\sin\left(\frac{\pi}{4}-\omega\right)-F\cos\left(\frac{\pi}{4}-\omega\right)\right)+\left(\frac{1}{2}-\frac{1}{2}\sin 2\omega\right)\frac{M}{l}\\&+(P\cos 2\omega+W\sin 2\omega)\left(\frac{7}{24}-\frac{5}{8}\sin 2\omega+\left(\frac{3}{8}+\frac{1}{24r}\right)\sin^2 2\omega\right)\\&+(P\sin 2\omega-W\cos 2\omega)\left(\frac{1}{4}+\frac{5}{16}\cos 2\omega-\frac{1}{4}\sin 2\omega-(\frac{3}{16}+\frac{1}{48r})\sin 4\omega\right)\Bigg]\sin\omega\end{aligned} \tag{A.21}$$

$$\begin{aligned}A_3=\Bigg[&(P\sin 2\omega-W\cos 2\omega)\left(\frac{1}{8}+\frac{1}{24r}\cos^2 2\omega\right)\\&+(P\cos 2\omega+W\sin 2\omega)\left(-\frac{1}{6}\cos 2\omega-\left(\frac{1}{8}+\frac{1}{24r}\right)\sin 2\omega\cos 2\omega\right)\\&-\frac{3}{16}\cos 2\omega\left(F\sin\left(\frac{\pi}{4}-\omega\right)+T\cos\left(\frac{\pi}{4}-\omega\right)\right)+\frac{1}{4}\frac{M}{l}\cos 2\omega+\frac{1}{8}T_3\cos 2\omega\\&-\frac{1}{16}T_4\cos 2\omega+\frac{3}{16}T_1\cos 2\omega-\frac{1}{4}T_2\cos 2\omega+\frac{1}{4}\frac{M_1}{l}\cos 2\omega\Bigg]\cos\omega\end{aligned} \tag{A.22}$$

$$\begin{aligned}A_4=\Bigg[&\left(-\frac{3}{16}-\frac{1}{8}\cos 2\omega\right)T_4+\left(\frac{5}{48}+\frac{1}{16}\cos 2\omega\right)T_3+\left(-\frac{1}{2}-\frac{11}{16}\cos 2\omega\right)T_6\\&+\left(\frac{1}{3}+\frac{1}{4}\cos 2\omega\right)T_5+\left(\frac{1}{2}+\frac{3}{4}\cos 2\omega\right)\frac{M_2}{l}\\&+\left(\frac{1}{3}+\frac{1}{4}\cos 2\omega\right)\left(T\sin\left(\frac{\pi}{4}-\omega\right)-F\cos\left(\frac{\pi}{4}-\omega\right)\right)+\left(-\frac{1}{2}-\frac{1}{2}\cos 2\omega\right)\frac{M}{l}\\&+(P\cos 2\omega+W\sin 2\omega)\left(-\frac{1}{4}+\frac{1}{4}\sin 2\omega-\frac{5}{16}\cos 2\omega+\left(\frac{3}{16}+\frac{1}{48r}\right)\sin 4\omega\right)\\&+(P\sin 2\omega-W\cos 2\omega)\left(-\frac{1}{3}-\frac{1}{2}\cos 2\omega-(\frac{3}{8}+\frac{1}{24r})\cos^2 2\omega\right)\Bigg]\cos\omega\end{aligned} \tag{A.23}$$

Combining Eqs. (A.7) to (A.14), (A.16) and (A.19), the 5 reduced equations in the unknowns (P, W, T_1, T_2, M_1) are

$$-4T_1-8\frac{M_1}{l}+\left(2\sin^2\omega-3\right)P+(2-\sin 2\omega)W+\left(2\sqrt{2}\cos\left(2\omega+\frac{\pi}{4}\right)+2\right)\bar{\sigma}l=0, \tag{A.24}$$

$$4T_1-2T_2+8\frac{M_1}{l}+2P-W+(\sin 2\omega-2\cos 2\omega-2)\,\bar{\sigma}l=0, \tag{A.25}$$

$$\left(-\frac{8}{r}-16\right)T_1+\left(-\frac{4}{r}-8\right)P+\left(\frac{4}{r}\cos 2\omega+\frac{4}{r}-\sin 2\omega+8\cos 2\omega+8\right)\bar{\sigma}l=0, \tag{A.26}$$

$$-18T_1+2T_2-36\frac{M_1}{l}+(-3\cos 2\omega-9)\,P+(-3\sin 2\omega+8)\,W + (-8\sin 2\omega+9\cos 2\omega+9)\,\bar{\sigma}l=0, \tag{A.27}$$

$$(-9\sin\omega+12\cos\omega)\,T_1+(3\sin\omega-6\cos\omega)\,T_2+(-18\sin\omega+24\cos\omega)\,\frac{M_1}{l} \left(\sin^3\omega-5\sin\omega+6\cos\omega\right)P+\left(\frac{2}{r}\cos\omega+3\sin\omega+\cos^3\omega\right)W + \left(5\sin 2\omega\cos\omega-6\cos^3\omega-6\cos\omega\right)\bar{\sigma}l=0. \tag{A.28}$$

Upon solving these five equations we obtain the explicit formulae:

$$P=-\frac{5r\bar{\sigma}l}{4\,(1+2r)}\tan 2\omega\sin 2\omega, \tag{A.29}$$

$$W=\frac{5r\bar{\sigma}l}{4\,(1+2r)}\sin 2\omega, \tag{A.30}$$

$$T_1=\frac{\bar{\sigma}lr\sin 2\omega}{8(1+2r)}(5\tan 2\omega-1)+\bar{\sigma}l\cos^2\omega, \tag{A.31}$$

$$T_2=-\frac{\bar{\sigma}l\,(4+3r)\sin 2\omega}{8(1+2r)}, \tag{A.32}$$

$$\frac{M_1}{l}=-\frac{2+r}{8(1+2r)}\bar{\sigma}l\sin 2\omega. \tag{A.33}$$

All other forces and moments follow immediately by back-substitution.

In order to obtain the macroscopic strain, we consider the unit cell from the original lattice as shown in Fig. A4. The non-vanishing strain components in the x-y coordinate system are

$$\bar{\epsilon}_{xx}=\frac{u_{P_5x}-u_{P_1x}}{2l\cos\omega}, \tag{A.34}$$

$$\bar{\epsilon}_{yy}=\frac{u_{P_9y}-u_{P_1y}}{2l\cos\omega}. \tag{A.35}$$

and, upon making use of gliding reflection symmetry for points in S_2, the strain components read

$$\bar{\epsilon}_{xx}=\frac{1}{2l\cos\omega}\left(u_{P_5x}-u_{P_2x}+u_{P_2x}-u_{P_1x}\right)=\frac{1}{l\cos\omega}\left(u_{P_2x}-u_{P_1x}\right), \tag{A.36}$$

$$\bar{\epsilon}_{yy}=\frac{1}{2l\cos\omega}\left(u_{P_9y}-u_{P_4y}+u_{P_4y}-u_{P_1y}\right)=\frac{1}{l\cos\omega}\left(u_{P_4y}-u_{P_1y}\right) \tag{A.37}$$

When P_2 is fixed, we have $u_{P_2x} = u_{P_2y} = 0$, and the displacements in Eqs. (A.36) and (A.37) in the x''- y'' coordinate system are

$$u_{P_1x} = -u_{P_1x''}\sin\omega - u_{P_1y''}\cos\omega = -u_{P_1x''}\sin\omega \tag{A.38}$$

$$u_{P_1y} = u_{P_1x''}\cos\omega - u_{P_1y''}\sin\omega = u_{P_1x''}\cos\omega \tag{A.39}$$

$$u_{P_4y} = u_{P_4x''}\cos\omega - u_{P_4y''}\sin\omega = u_{P_1x''}\cos\omega - u_{P_4y''}\sin\omega \tag{A.40}$$

Consequently,

$$\bar{\epsilon}_{xx} = \frac{u_{P_1x''}\tan\omega}{l}, \tag{A.41}$$

$$\bar{\epsilon}_{yy} = -\frac{u_{P_4y''}\tan\omega}{l}. \tag{A.42}$$

Now, the displacements in the x''- y'' coordinate system are

$$u_{P_1x''} = \frac{l^3}{E_BI_B}\left[-\frac{5}{48}\left(P\cos 2\omega + W\sin 2\omega\right) - \frac{3}{16}W - \frac{1}{3}\left(F\sin\left(\frac{\pi}{4}-\omega\right) + T\cos\left(\frac{\pi}{4}-\omega\right)\right)\right.$$
$$\left. + \frac{M}{2l} + \frac{1}{4}T_3 - \frac{1}{12}T_4 + \frac{1}{3}T_1 - \frac{1}{2}T_2 + \frac{M_1}{2l}\right] = \frac{(8+3r)\sin 2\omega}{192(1+2r)}\frac{\bar{\sigma}l^4}{E_BI_B}, \tag{A.43}$$

$$u_{P_4y''} = \frac{l^3}{E_BI_B}\left[\frac{1}{8}\left(P\cos 2\omega + W\sin 2\omega\right) + \frac{1}{4}W + \frac{1}{2}\left(F\sin\left(\frac{\pi}{4}-\omega\right) + T\cos\left(\frac{\pi}{4}-\omega\right)\right)\right.$$
$$\left. - \frac{M}{l} - \frac{29}{48}T_3 - \frac{3}{16}T_4 - \frac{1}{2}T_1 + \frac{4}{3}T_2 - \frac{3M_1}{2l}\right] = -\frac{(8+3r)\sin 2\omega}{192(1+2r)}\frac{\bar{\sigma}l^4}{E_BI_B}. \tag{A.44}$$

Consequently, both macroscopic strain components are given by the simple, explicit formula

$$\bar{\epsilon}_{xx} = \bar{\epsilon}_{yy} = \frac{(8+3r)\sin^2\omega}{96\,(1+2r)}\frac{\bar{\sigma}l^3}{E_BI_B}. \tag{A.45}$$

The bulk modulus follows as

$$\frac{\bar{K}}{E_B\bar{t}_B^3} = \frac{\bar{\sigma}}{2\bar{\epsilon}_{xx}E_B\bar{t}_B^3} = \frac{4\,(1+2r)}{(8+3r)\sin^2\omega} \tag{A.46}$$

where

$$\bar{t}_B = \frac{t_B}{l}. \tag{A.47}$$

Now make use of the relative density of the structure as defined by

$$\bar{\rho} = \frac{2t_B + t_A}{l\cos^2\omega} \tag{A.48}$$

and introduce the reference relative density

$$\bar{\rho}_{\text{ref}} = \bar{\rho}\cos^2\omega|_{t_A=0} = 2\bar{t}_B. \tag{A.49}$$

The bulk modulus can then be written as

$$\frac{\bar{K}}{E_B \bar{\rho}_{\text{ref}}^3} = \frac{1+2r}{2\,(8+3r)\sin^2\omega}. \tag{A.50}$$

Appendix A.2. Shear loading

Under shear loading, the stress state in the x-y plane is expressed as ($\bar{\sigma}_{xx} = \bar{\sigma}_{yy} = 0$, $\bar{\sigma}_{xy} = \bar{\tau}$) or, under transformation to the x'- y' coordinate system, as ($\bar{\sigma}'_{xx} = \bar{\tau}$, $\bar{\sigma}'_{yy} = -\bar{\tau}$, $\bar{\sigma}'_{xy} = 0$).

We proceed by making use of the symmetry of the structure as shown in Fig. A5(a,b). Reflection about the $y' = x'$ axis of Fig. A5(a), generates the same structure, but the loading condition reverses and all reaction forces/moments alternate in sign. We make use of this fact and identify the five unknowns (F, M, T, P, W), as shown in Fig. A2(c), with $M = 0$ by symmetry. A similar analysis to the equi-biaxial loading case provides:

$$F = -\frac{\sqrt{2}}{2} P \sin\omega + \frac{\sqrt{2}}{2} W \cos\omega + \sqrt{2}\bar{\tau} l \cos\omega \tag{A.51}$$

$$T = \frac{\sqrt{2}}{2} P \sin\omega - \frac{\sqrt{2}}{2} W \cos\omega \tag{A.52}$$

Now introduce the same cut as in the case of equi-biaxial loading, as shown in Fig. A6. Equilibrium demands:

$$T_3 = 2T_2 + W + 2\bar{\tau} l \cos^2\omega \tag{A.53}$$

$$T_4 = 2T_1 - P + \bar{\tau} l \sin 2\omega \tag{A.54}$$

$$T_5 = -T_2 + P \sin\omega\cos\omega - W\cos^2\omega - \sqrt{2}\bar{\tau} l \cos\omega \sin\left(\frac{\pi}{4} - \omega\right) \tag{A.55}$$

$$T_6 = T_1 + P\sin^2\omega - W\cos\omega\sin\omega - \sqrt{2}\bar{\tau} l \cos\omega\cos\left(\frac{\pi}{4} - \omega\right) \tag{A.56}$$

$$M_2 = M_1 \tag{A.57}$$

Thus five unknowns (P, W, T_1, T_2, M_1) remain. Based on symmetry and continuation condition, we have four equations that are independent:

$$\theta_{P_1} = 0 \tag{A.58}$$

$$\theta_{P_3} = 0 \tag{A.59}$$

$$u_{P_{C1}x''} - u_{P_{C2}x''} = 0 \tag{A.60}$$

$$u_{P_{C1}y''} - u_{P_{C2}y''} = 0 \tag{A.61}$$

These four equations are identical to Eqs. (A.12) to (A.14) and (A.16). The fifth equation is expressed as

$$u_{P_{C4}y} - u_{P_{C3}y} = 0. \tag{A.62}$$

In the x''- y'' coordinate system, this equation leads to

$$\begin{aligned} &- \left(u_{P_{C3}x''} - u_{P_{C4}x''}\right)\cos\omega + \left(u_{P_{C3}y''} - u_{P_{C4}y''}\right)\sin\omega \\ &\qquad = \frac{l^3}{E_B I_B}\left[-B_1 + B_2 + B_3 - B_4\right] \end{aligned} \tag{A.63}$$

where

$$\begin{aligned} B_1 = &\left[\left(P\sin 2\omega - W\cos 2\omega\right)\left(\frac{1}{16}\cos 2\omega + \left(\frac{1}{8} + \frac{1}{48r}\sin 4\omega\right)\right)\right. \\ &+ \left(P\cos 2\omega + W\sin 2\omega\right)\left(-\frac{1}{24} - \frac{1}{8}\sin 2\omega - \left(\frac{1}{8} + \frac{1}{24r}\right)\sin^2 2\omega\right) \\ &- \left(\frac{5}{48} + \frac{3}{16}\sin 2\omega\right)\left(F\sin\left(\frac{\pi}{4} - \omega\right) + T\cos\left(\frac{\pi}{4} - \omega\right)\right) \\ &+ \left(\frac{1}{8} + \frac{1}{4}\sin 2\omega\right)\frac{M}{l} + \left(\frac{1}{16} + \frac{1}{8}\sin 2\omega\right)T_3 - \left(\frac{1}{24} + \frac{1}{16}\sin 2\omega\right)T_4 \\ &+ \left(\frac{5}{48} + \frac{3}{16}\sin 2\omega\right)T_1 - \left(\frac{1}{8} + \frac{1}{4}\sin 2\omega\right)T_2 \\ &\left.+ \left(\frac{1}{8} + \frac{1}{4}\sin 2\omega\right)\frac{M_1}{l}\right]\cos\omega \end{aligned} \tag{A.64}$$

$$\begin{aligned} B_2 = &\left[\left(\frac{1}{8} - \frac{1}{8}\sin 2\omega\right)T_4 + \left(-\frac{1}{16} + \frac{1}{16}\sin 2\omega\right)T_3\right. \\ &+ \left(\frac{29}{48} - \frac{11}{16}\sin 2\omega\right)T_6 + \left(-\frac{1}{4} + \frac{1}{4}\sin 2\omega\right)T_5 + \left(-\frac{5}{8} + \frac{3}{4}\sin 2\omega\right)\frac{M_2}{l} \\ &+ \left(-\frac{1}{4} + \frac{1}{4}\sin 2\omega\right)\left(T\sin\left(\frac{\pi}{4} - \omega\right) - F\cos\left(\frac{\pi}{4} - \omega\right)\right) + \left(\frac{1}{2} - \frac{1}{2}\sin 2\omega\right)\frac{M}{l} \\ &+ \left(P\cos 2\omega + W\sin 2\omega\right)\left(\frac{7}{24} - \frac{5}{8}\sin 2\omega + \left(\frac{3}{8} + \frac{1}{24r}\right)\sin^2 2\omega\right) \\ &\left.+ \left(P\sin 2\omega - W\cos 2\omega\right)\left(\frac{1}{4} + \frac{5}{16}\cos 2\omega - \frac{1}{4}\sin 2\omega - (\frac{3}{16} + \frac{1}{48r})\sin 4\omega\right)\right]\cos\omega \end{aligned} \tag{A.65}$$

$$\begin{aligned} B_3 = &\left[\left(P\sin 2\omega - W\cos 2\omega\right)\left(\frac{1}{8} + \frac{1}{24r}\cos^2 2\omega\right)\right. \\ &\left.+ \left(P\cos 2\omega + W\sin 2\omega\right)\left(-\frac{1}{6}\cos 2\omega - \left(\frac{1}{8} + \frac{1}{24r}\right)\sin 2\omega\cos 2\omega\right)\right. \end{aligned}$$

$$
\begin{aligned}
&- \frac{3}{16}\cos 2\omega \left(F \sin\left(\frac{\pi}{4}-\omega\right) + T\cos\left(\frac{\pi}{4}-\omega\right)\right) + \frac{1}{4}\frac{M}{l}\cos 2\omega + \frac{1}{8}T_3\cos 2\omega \\
&-\frac{1}{16}T_4\cos 2\omega + \frac{3}{16}T_1\cos 2\omega - \frac{1}{4}T_2\cos 2\omega + \frac{1}{4}\frac{M_1}{l}\cos 2\omega\Big]\sin\omega \qquad \text{(A.66)}\\
B_4 = &\Bigg[\left(-\frac{3}{16}-\frac{1}{8}\cos 2\omega\right)T_4 + \left(\frac{5}{48}+\frac{1}{16}\cos 2\omega\right)T_3 + \left(-\frac{1}{2}-\frac{11}{16}\cos 2\omega\right)T_6 \\
&+\left(\frac{1}{3}+\frac{1}{4}\cos 2\omega\right)T_5 + \left(\frac{1}{2}+\frac{3}{4}\cos 2\omega\right)\frac{M_2}{l} \\
&+\left(\frac{1}{3}+\frac{1}{4}\cos 2\omega\right)\left(T\sin\left(\frac{\pi}{4}-\omega\right) - F\cos\left(\frac{\pi}{4}-\omega\right)\right) + \left(-\frac{1}{2}-\frac{1}{2}\cos 2\omega\right)\frac{M}{l} \\
&+(P\cos 2\omega + W\sin 2\omega)\left(-\frac{1}{4}+\frac{1}{4}\sin 2\omega - \frac{5}{16}\cos 2\omega + \left(\frac{3}{16}+\frac{1}{48r}\right)\sin 4\omega\right) \\
&+(P\sin 2\omega - W\cos 2\omega)\left(-\frac{1}{3}-\frac{1}{2}\cos 2\omega - (\frac{3}{8}+\frac{1}{24r})\cos^2 2\omega\right)\Bigg]\sin\omega \qquad \text{(A.67)}
\end{aligned}
$$

Now rearrange the five equations and take into account Eqs. (A.53) to (A.57), to obtain a reduced set of 5 relations

$$
-4T_1 - 8\frac{M_1}{l} + \left(2\sin^2\omega + 1\right)P + (-2-\sin 2\omega)W + \left(-2\sqrt{2}\sin\left(2\omega+\frac{\pi}{4}\right) - 2\right)\bar{\tau}l = 0, \qquad \text{(A.68)}
$$

$$
4T_1 - 2T_2 + 8\frac{M_1}{l} - 2P + W + (2\sin 2\omega + \cos 2\omega + 1)\,\bar{\tau}l = 0, \qquad \text{(A.69)}
$$

$$
\left(-\frac{4}{r}-8\right)T_1 + \left(\frac{2}{r}+4\right)P - 3W + \left(-\frac{2}{r}\sin 2\omega - 4\sin 2\omega - 5\cos^2\omega\right)\bar{\tau}l = 0, \qquad \text{(A.70)}
$$

$$
\begin{aligned}
&-9T_1 + T_2 - 18\frac{M_1}{l} + \left(3\sin^2\omega + 3\right)P + (-3\sin\omega\cos\omega - 4)\,W \\
&\quad + \left(-9\sin\omega\cos\omega - 8\cos^2\omega\right)\bar{\tau}l = 0, \qquad \text{(A.71)}
\end{aligned}
$$

$$
\begin{aligned}
&(6\sin\omega - 9\cos\omega)\,T_1 + 3\cos\omega T_2 - 18\cos\omega\frac{M_1}{l} + \left(\sin^2\omega\cos\omega - 3\sin\omega + 4\cos\omega\right)P \\
&\quad + \left(\frac{2}{r}\sin\omega - \sin\omega\cos^2\omega + 4\sin\omega - 3\cos\omega\right)W + (-6\cos 2\omega\cos\omega - 2\sin 2\omega\cos\omega)\,\bar{\tau}l = 0. \qquad \text{(A.72)}
\end{aligned}
$$

Upon solving these five equations we obtain

$$
P = -W\tan 2\omega, \qquad \text{(A.73)}
$$

$$
W = -\frac{5r}{2+7r}\bar{\tau}l\cos^2\omega, \qquad \text{(A.74)}
$$

$$
T_1 = \frac{1}{2}P - \frac{1}{2}\left(\frac{5r\cos^2\omega}{2+7r} - \sin 2\omega\right)\bar{\tau}l, \qquad \text{(A.75)}
$$

$$T_2 = -\frac{4+9r}{2(2+7r)}\bar{\tau} l \cos^2\omega, \tag{A.76}$$

$$\frac{M_1}{l} = -\frac{1+r}{2+7r}\bar{\tau} l \cos^2\omega. \tag{A.77}$$

$$\tag{A.78}$$

As the case of equi-biaxial loading, the strain components in the x-y coordinate system is expressed as ($\bar{\epsilon}_{xx} = \bar{\epsilon}_{yy} = 0$)

$$\bar{\epsilon}_{xy} = \frac{u_{P_5 y} - u_{P_1 y}}{2l\cos\omega} = \frac{1}{l\cos\omega}\left(u_{P_2 y} - u_{P_1 y}\right), \text{ and} \tag{A.79}$$

$$\bar{\epsilon}_{yx} = \bar{\epsilon}_{xy} = \frac{u_{P_9 x} - u_{P_1 x}}{2l\cos\omega} = \frac{1}{l\cos\omega}\left(u_{P_4 x} - u_{P_1 x}\right) \tag{A.80}$$

If we fix P_2 so that $u_{P_2 x} = u_{P_2 y} = 0$, we obtain

$$\bar{\epsilon}_{xy} = \frac{1}{l\cos\omega}\left(u_{P_2 y} - u_{P_1 y}\right) = -\frac{u_{P_1 x''}}{l}, \text{ and} \tag{A.81}$$

$$\bar{\epsilon}_{yx} = \frac{1}{l\cos\omega}\left(u_{P_4 x} - u_{P_1 x}\right) = -\frac{u_{P_4 y''}}{l}. \tag{A.82}$$

The displacements in the x''- y'' coordinate system are

$$u_{P_1 x''} = \frac{l^3}{E_B I_B}\left[-\frac{5}{48}\left(P\cos 2\omega + W\sin 2\omega\right) - \frac{3}{16}W - \frac{1}{3}\left(F\sin\left(\frac{\pi}{4}-\omega\right) + T\cos\left(\frac{\pi}{4}-\omega\right)\right)\right.$$
$$\left. + \frac{M}{2l} + \frac{1}{4}T_3 - \frac{1}{12}T_4 + \frac{1}{3}T_1 - \frac{1}{2}T_2 + \frac{M_1}{2l}\right], \tag{A.83}$$

$$u_{P_4 y''} = \frac{l^3}{E_B I_B}\left[\frac{1}{8}\left(P\cos 2\omega + W\sin 2\omega\right) + \frac{1}{4}W + \frac{1}{2}\left(F\sin\left(\frac{\pi}{4}-\omega\right) + T\cos\left(\frac{\pi}{4}-\omega\right)\right)\right.$$
$$\left. - \frac{M}{l} - \frac{29}{48}T_3 - \frac{3}{16}T_4 - \frac{1}{2}T_1 + \frac{4}{3}T_2 - \frac{3M_1}{2l}\right], \tag{A.84}$$

which reduce to

$$u_{P_1 x''} = u_{P_4 y''} = -\frac{(8+3r)\cos^2\omega}{48(2+7r)}\frac{\bar{\tau} l^4}{E_B I_B}. \tag{A.85}$$

upon eliminating (P, W, F, T, M). The shear strains are then

$$\bar{\epsilon}_{xy} = \bar{\epsilon}_{yx} = \frac{(8+3r)\cos^2\omega}{48\,(2+7r)}\frac{\bar{\tau} l^3}{E_B I_B} \tag{A.86}$$

The macroscopic shear modulus follows immediately as

$$\frac{\bar{G}_{xy}}{E_B \bar{\rho}_{\text{ref}}^3} = \frac{\bar{\tau}}{2\bar{\epsilon}_{xy} E_B \bar{\rho}_{\text{ref}}^3} = \frac{2+7r}{4\,(8+3r)\cos^2\omega} \tag{A.87}$$

where $\bar{\rho}_{\text{ref}}$ has already been defined in Eq. (9).

References

Amanieu, H.Y., Rosato, D., Sebastiani, M., Massimi, F., Lupascu, D.C., 2014. Mechanical property measurements of heterogeneous materials by selective nanoindentation: Application to $LiMn_2O_4$ cathode. Materials Science and Engineering: A 593, 92–102. https://dx.doi.org/10.1016/j.msea.2013.11.044.

Amin, R., Chiang, Y.M., 2016. Characterization of Electronic and Ionic Transport in $Li_{1-x}Ni_{0.33}Mn_{0.33}Co_{0.33}O_2$ (NMC333) and $Li_{1-x}Ni_{0.50}Mn_{0.20}Co_{0.30}O_2$ (NMC523) as a Function of Li Content. Journal of The Electrochemical Society 163, A1512–A1517. https://dx.doi.org/10.1149/2.0131608jes.

Aono, H., Sugimoto, E., Sadaoka, Y., Imanaka, N., Adachi, G.y., 1989. Ionic Conductivity of the Lithium Titanium Phosphate ($Li_{1+X}M_XTi_{2-X}(PO_4)_3$, M = Al, Sc, Y, and La) Systems. Journal of The Electrochemical Society 136, 590–591. https://dx.doi.org/10.1149/1.2096693.

Bachman, J.C., Muy, S., Grimaud, A., Chang, H.H., Pour, N., Lux, S.F., Paschos, O., Maglia, F., Lupart, S., Lamp, P., Giordano, L., Shao-Horn, Y., 2016. Inorganic Solid-State Electrolytes for Lithium Batteries: Mechanisms and Properties Governing Ion Conduction. Chemical Reviews 116, 140–162. https://dx.doi.org/10.1021/acs.chemrev.5b00563.

Bhandakkar, T.K., Johnson, H.T., 2012. Diffusion induced stresses in buckling battery electrodes. Journal of the Mechanics and Physics of Solids 60, 1103–1121. https://dx.doi.org/10.1016/j.jmps.2012.02.012.

Deng, Z., Wang, Z., Chu, I.H., Luo, J., Ong, S.P., 2016. Elastic Properties of Alkali Superionic Conductor Electrolytes from First Principles Calculations. Journal of The Electrochemical Society 163, A67–A74. https://dx.doi.org/10.1149/2.0061602jes.

Famprikis, T., Canepa, P., Dawson, J.A., Islam, M.S., Masquelier, C., 2019. Fundamentals of inorganic solid-state electrolytes for batteries. Nature Materials , 1–14https://dx.doi.org/10.1038/s41563-019-0431-3.

Fergus, J.W., 2010. Ceramic and polymeric solid electrolytes for lithium-ion batteries. Journal of Power Sources 195, 4554–4569. https://dx.doi.org/10.1016/j.jpowsour.2010.01.076.

Janek, J., Zeier, W.G., 2016. A solid future for battery development. Nature Energy 1, 1–4. https://dx.doi.org/10.1038/nenergy.2016.141.

Kato, Y., Hori, S., Saito, T., Suzuki, K., Hirayama, M., Mitsui, A., Yonemura, M., Iba, H., Kanno, R., 2016. High-power all-solid-state batteries using sulfide superionic conductors. Nature Energy 1, 1–7. https://dx.doi.org/10.1038/nenergy.2016.30.

Koerver, R., Zhang, W., Biasi, L.d., Schweidler, S., Kondrakov, A.O., Kolling, S., Brezesinski, T., Hartmann, P., Zeier, W.G., Janek, J., 2018. Chemo-mechanical expansion of lithium electrode materials—on the route to mechanically optimized all-solid-state batteries. Energy & Environmental Science 11, 2142–2158. https://dx.doi.org/10.1039/C8EE00907D.

Koyama, Y., Chin, T.E., Rhyner, U., Holman, R.K., Hall, S.R., Chiang, Y.M., 2006. Harnessing the Actuation Potential of Solid-State Intercalation Compounds. Advanced Functional Materials 16, 492–498. https://dx.doi.org/10.1002/adfm.200500633.

Lakes, R., 1996. Cellular solid structures with unbounded thermal expansion. Journal of Materials Science Letters 15, 475–477. https://dx.doi.org/10.1007/BF00275406.

Lakes, R., 2007. Cellular solids with tunable positive or negative thermal expansion of unbounded magnitude. Applied Physics Letters 90, 221905. https://dx.doi.org/10.1063/1.2743951.

Liu, Z., Fu, W., Payzant, E.A., Yu, X., Wu, Z., Dudney, N.J., Kiggans, J., Hong, K., Rondinone, A.J., Liang, C., 2013. Anomalous High Ionic Conductivity of Nanoporous $\beta-\mathrm{Li_3PS_4}$. Journal of the American Chemical Society 135, 975–978. https://dx.doi.org/10.1021/ja3110895.

McGrogan, F.P., Swamy, T., Bishop, S.R., Eggleton, E., Porz, L., Chen, X., Chiang, Y.M., Vliet, K.J.V., 2017. Compliant Yet Brittle Mechanical Behavior of $\mathrm{Li_2S-P_2S_5}$ Lithium-Ion-Conducting Solid Electrolyte. Advanced Energy Materials 7, 1602011. https://dx.doi.org/10.1002/aenm.201602011.

Mykhaylov, M., Ganser, M., Klinsmann, M., Hildebrand, F.E., Guz, I., McMeeking, R.M., 2019. An elementary 1-dimensional model for a solid state lithium-ion battery with a single ion

conductor electrolyte and a lithium metal negative electrode. Journal of the Mechanics and Physics of Solids 123, 207–221. https://dx.doi.org/10.1016/j.jmps.2018.10.004.

Nitta, N., Wu, F., Lee, J.T., Yushin, G., 2015. Li-ion battery materials: present and future. Materials Today 18, 252–264. https://dx.doi.org/10.1016/j.mattod.2014.10.040.

Park, M., Zhang, X., Chung, M., Less, G.B., Sastry, A.M., 2010. A review of conduction phenomena in Li-ion batteries. Journal of Power Sources 195, 7904–7929. https://dx.doi.org/10.1016/j.jpowsour.2010.06.060.

Qu, M., Woodford, W.H., Maloney, J.M., Carter, W.C., Chiang, Y.M., Van Vliet, K.J., 2012. Nanomechanical Quantification of Elastic, Plastic, and Fracture Properties of $LiCoO_2$. Advanced Energy Materials 2, 940–944. https://dx.doi.org/10.1002/aenm.201200107.

Sigmund, O., Torquato, S., 1996. Composites with extremal thermal expansion coefficients 69, 3203–3205. https://dx.doi.org/10.1063/1.117961. publisher: American Institute of Physics.

Sigmund, O., Torquato, S., 1997. Design of materials with extreme thermal expansion using a three-phase topology optimization method 45, 1037–1067. https://dx.doi.org/10.1016/S0022-5096(96)00114-7.

Steeves, C.A., dos Santos e Lucato, S.L., He, M., Antinucci, E., Hutchinson, J.W., Evans, A.G., 2007. Concepts for structurally robust materials that combine low thermal expansion with high stiffness. Journal of the Mechanics and Physics of Solids 55, 1803–1822. https://dx.doi.org/10.1016/j.jmps.2007.02.009.

Steeves, C.A., Mercer, C., Antinucci, E., He, M.Y., Evans, A.G., 2009. Experimental investigation of the thermal properties of tailored expansion lattices. International Journal of Mechanics and Materials in Design 5, 195–202. https://dx.doi.org/10.1007/s10999-009-9094-6.

Swallow, J.G., Woodford, W.H., McGrogan, F.P., Ferralis, N., Chiang, Y.M., Vliet, K.J.V., 2014. Effect of Electrochemical Charging on Elastoplastic Properties and Fracture Toughness of Li_XCoO_2. Journal of The Electrochemical Society 161, F3084–F3090. https://dx.doi.org/10.1149/2.0141411jes.

Taylor, R.L., 2017. FEAP - finite element analysis program (v8.5). http://www.ce.berkeley/feap.

Wolfenstine, J., Allen, J.L., Sakamoto, J., Siegel, D.J., Choe, H., 2018. Mechanical behavior of Li-ion-conducting crystalline oxide-based solid electrolytes: a brief review. Ionics 24, 1271–1276. https://dx.doi.org/10.1007/s11581-017-2314-4.

Wolfenstine, J., Jo, H., Cho, Y.H., David, I.N., Askeland, P., Case, E.D., Kim, H., Choe, H., Sakamoto, J., 2013. A preliminary investigation of fracture toughness of $Li_7La_3Zr_2O_{12}$ and its comparison to other solid Li-ionconductors. Materials Letters 96, 117–120. https://dx.doi.org/10.1016/j.matlet.2013.01.021.

Woodford, W.H., Carter, W.C., Chiang, Y.M., 2012. Design criteria for electrochemical shock resistant battery electrodes. Energy & Environmental Science 5, 8014–8024. https://dx.doi.org/10.1039/C2EE21874G.

Woodford, W.H., Chiang, Y.M., Carter, W.C., 2013. Electrochemical Shock in Ion-Intercalation Materials with Limited Solid-Solubility. Journal of The Electrochemical Society 160, A1286–A1292. https://dx.doi.org/10.1149/2.104308jes.

Xia, H., Meng, S.Y., Lu, L., Ceder, G., 2007. Electrochemical Behavior and Li Diffusion Study of $LiCoO_2$ Thin Film Electrodes Prepared by PLD http://dspace.mit.edu/handle/1721.1/35827.

Xu, R., Sun, H., Vasconcelos, L.S.d., Zhao, K., 2017. Mechanical and Structural Degradation of $LiNi_xMn_yCo_zO_2$ Cathode in Li-Ion Batteries: An Experimental Study. Journal of The Electrochemical Society 164, A3333–A3341. https://dx.doi.org/10.1149/2.1751713jes.

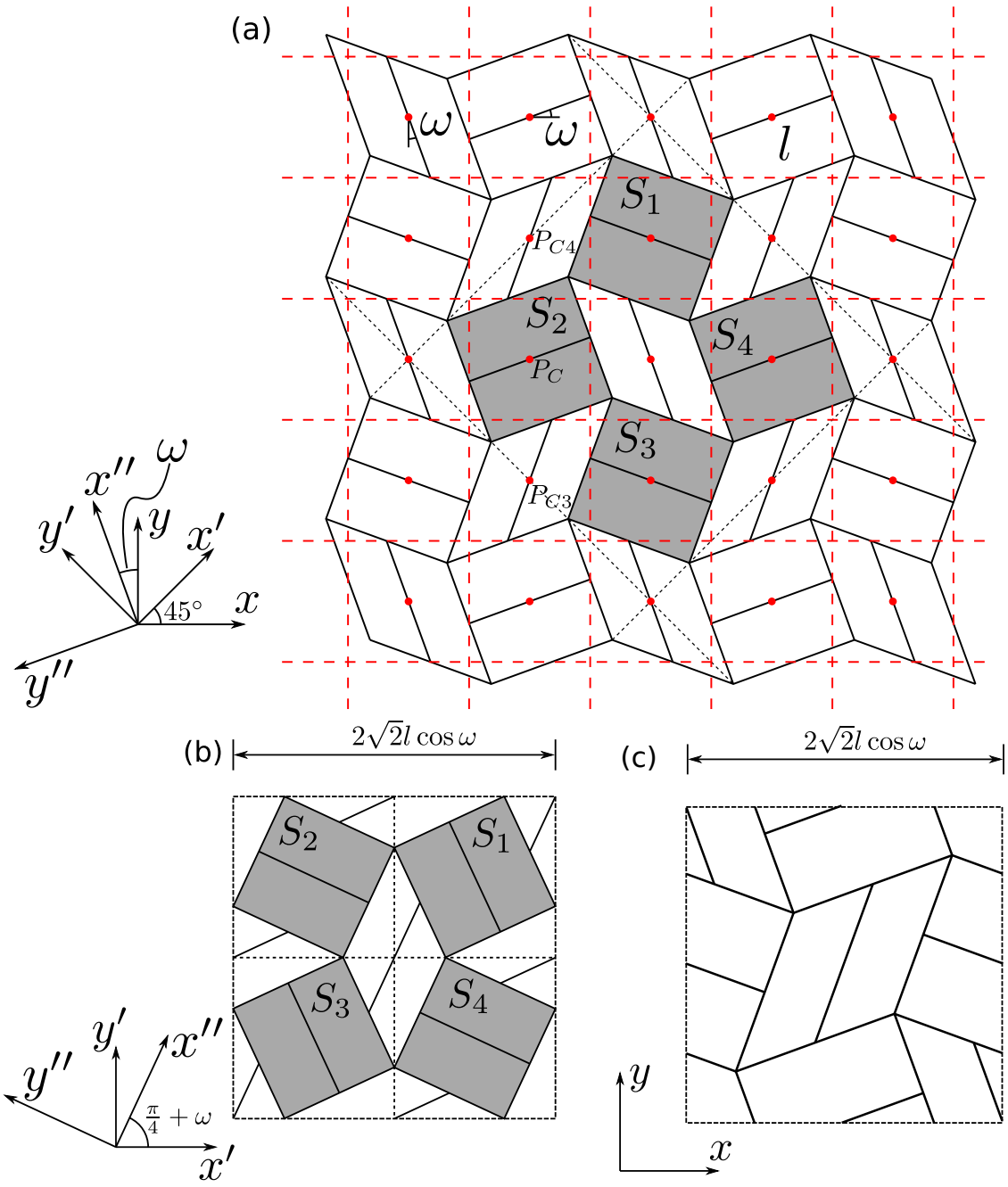

Figure A1: Simplified structure and its unit cell in a new coordinate system. (a) Sketch showing that the structure has two symmetries: $180°$ rotation symmetry with respect to red dots, e.g., P_C, P_{C3}, P_{C4}; gliding reflection symmetry with respect to red dashed lines. (b) The unit cell in the new coordinate system x'- y'. (c) The unit cell for an FE simulation.

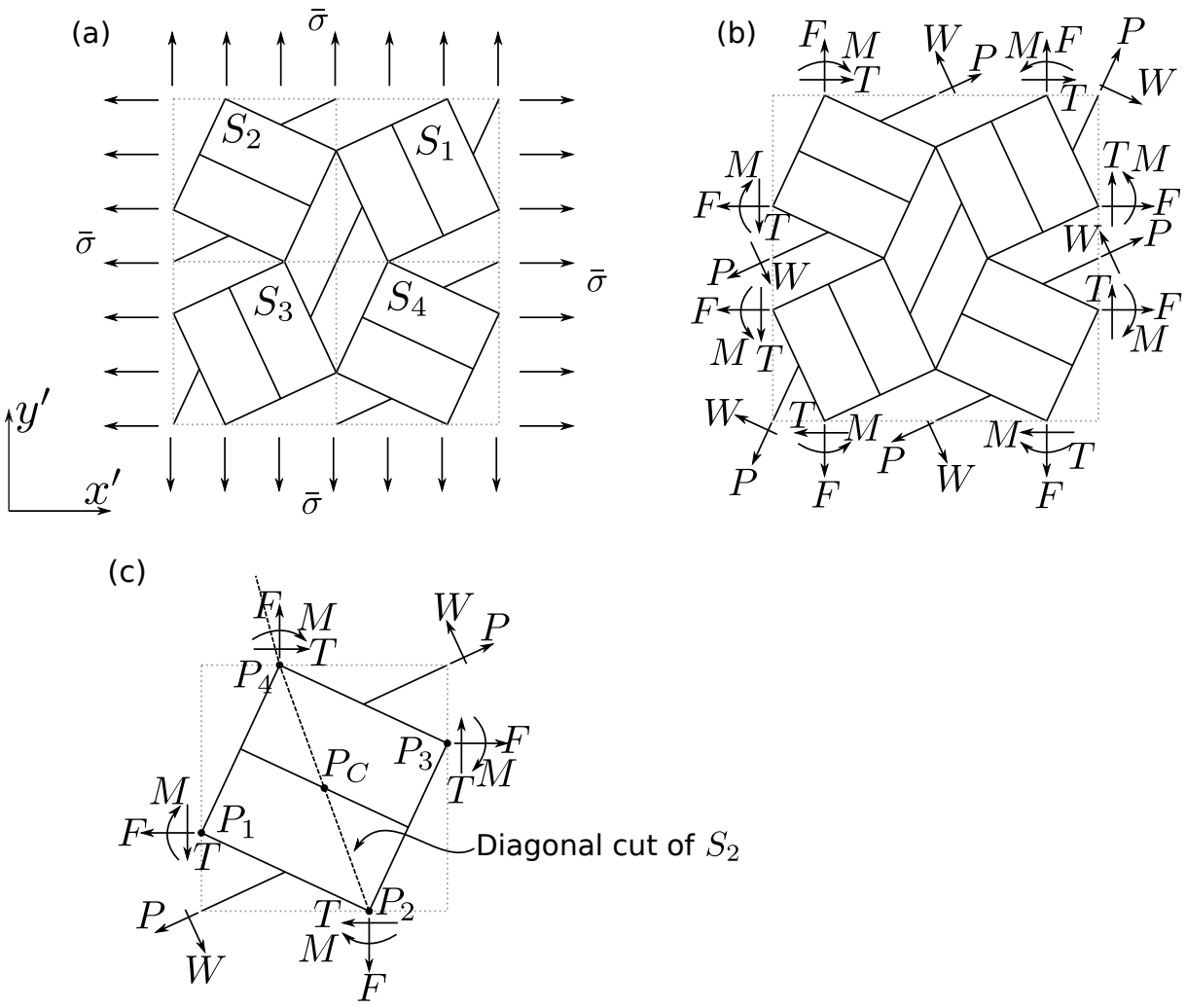

Figure A2: Illustration of hydrostatic loading and corresponding forces. (a) Stress state in the new coordinate system x'- y'. (b) Equivalent forces acting on the cross sections on the unit cell. (c) Forces analysis on one square S_2 of the unit cell.

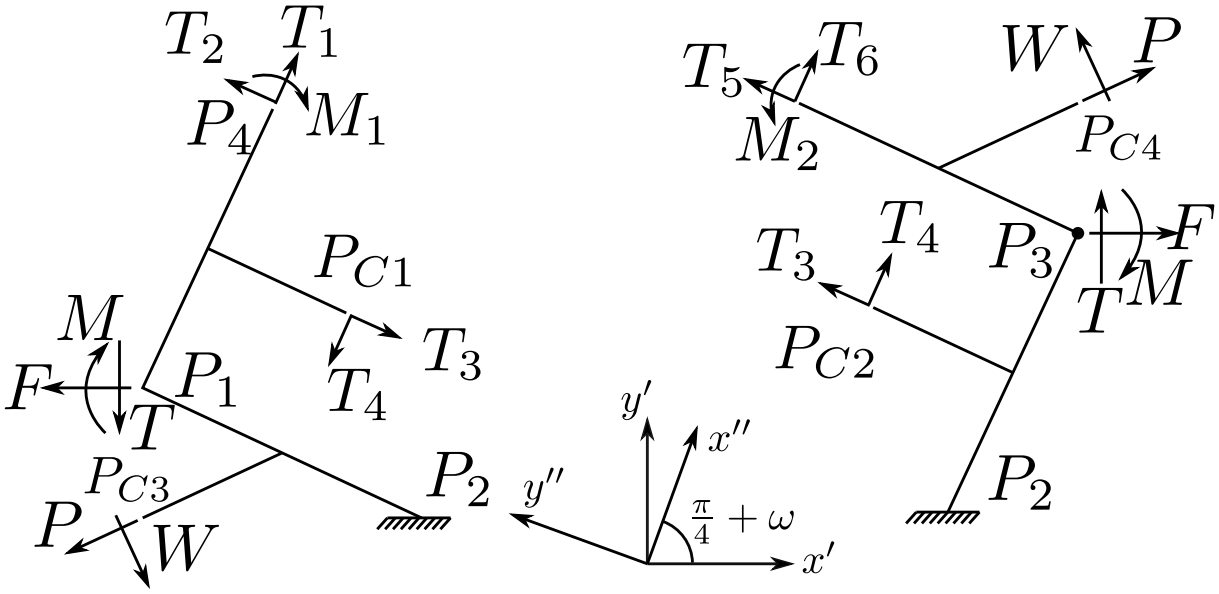

Figure A3: Diagonal cut of S_2 in the hydrostatic loading case.

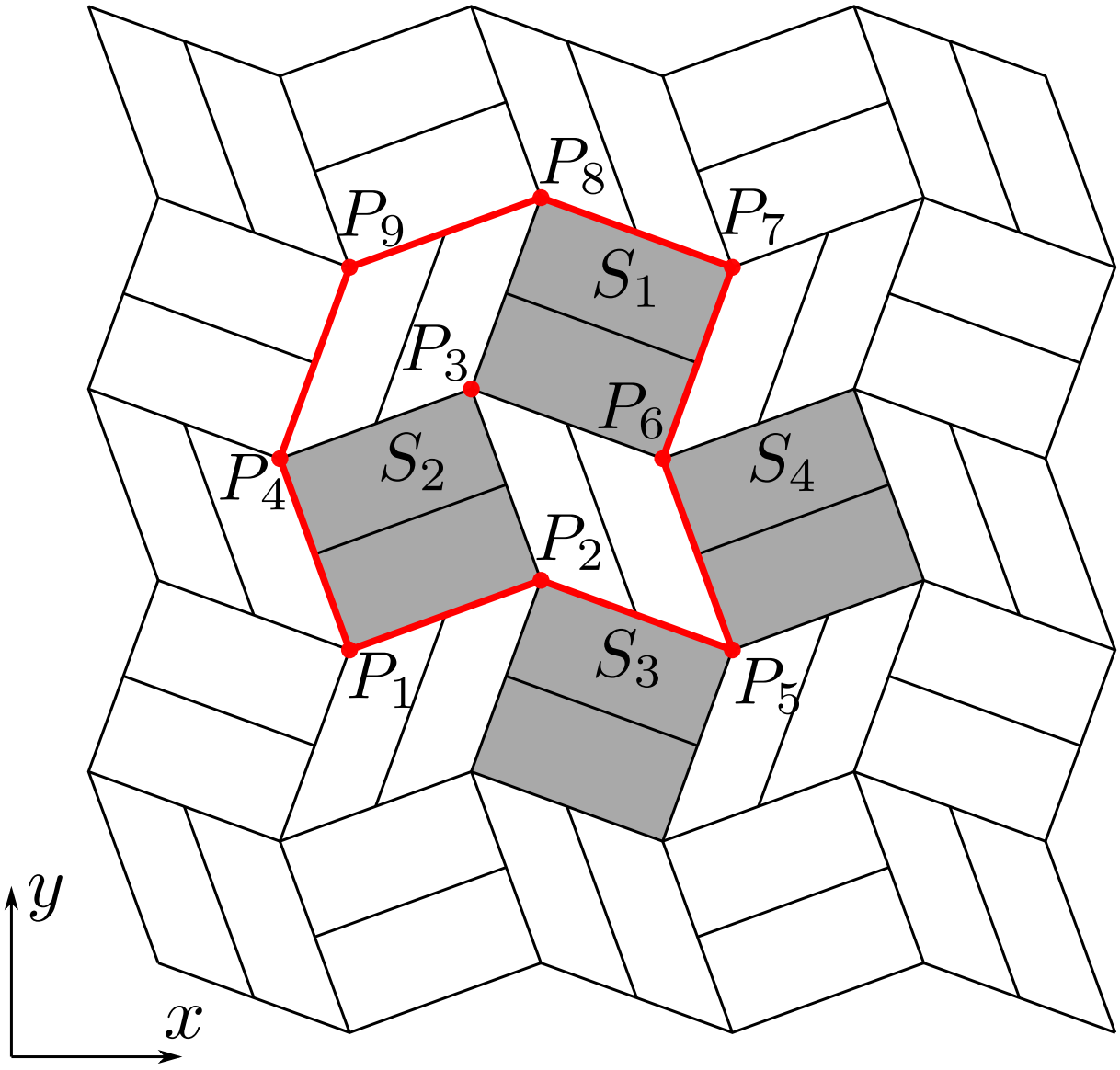

Figure A4: Unit cell for calculation of macroscopic strain, denoted within the red thick line. It contains two squares S_1 and S_2 and two diamonds. The nine vetices of the squares and diamonds are denoted by P_1–P_9.

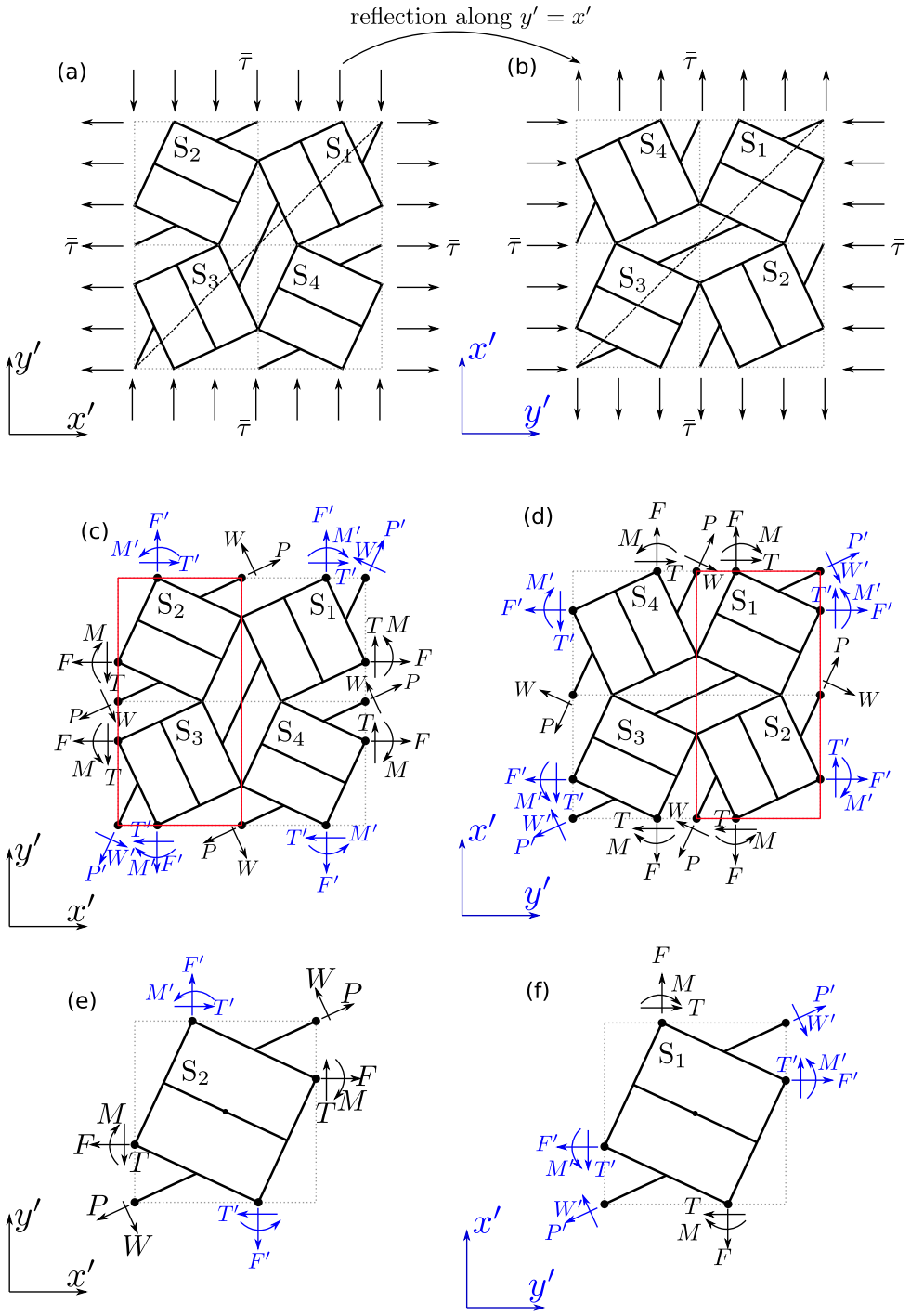

Figure A5: Forces analysis of the structure under pure shear. (a) The stress state under x'- y' coordinate system. (b) Sketch illustrating that when the structure undergoes a reflection operation along $y' = x'$, the structure remains the same, but the loading condition becomes its inverse. (c) Equivalent forces on the cross sections of the unit cell. (d) The forces on the reflected structure. A superposition of (c) and (d) results in zero macroscopic forces and thus forces in blue with prime are opposite of the corresponding forces in black without prime. (e, f) The forces on a square S_2 and S_1 of the unit cell.

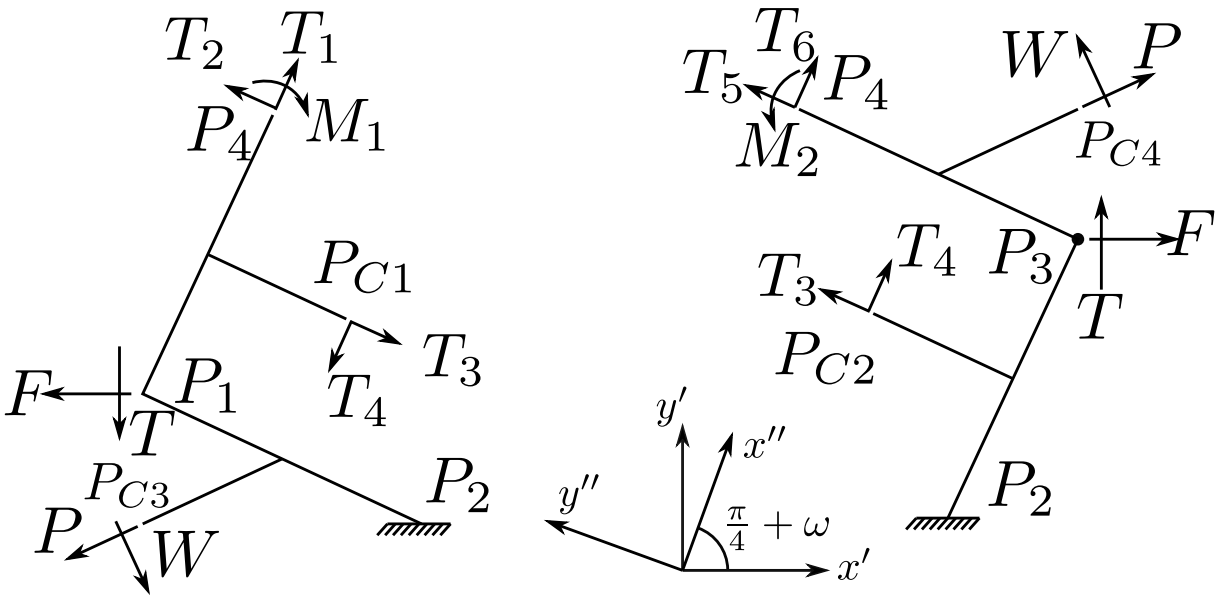

Figure A6: Diagonal cut of S_2.